PHYSICAL REVIEW D **92,** 114502 (2015)

Magnetic structure of light nuclei from lattice QCD

Emmanuel Chang,[1] William Detmold,[2] Kostas Orginos,[3,4] Assumpta Parreño,[5] Martin J. Savage,[1] Brian C. Tiburzi,[6,7,8] and Silas R. Beane[9]
(NPLQCD Collaboration)

[1]*Institute for Nuclear Theory, University of Washington, Seattle, Washington 98195-1550, USA*
[2]*Center for Theoretical Physics, Massachusetts Institute of Technology, Cambridge, Massachusetts 02139, USA*
[3]*Department of Physics, College of William and Mary, Williamsburg, Virginia 23187-8795, USA*
[4]*Jefferson Laboratory, 12000 Jefferson Avenue, Newport News, Virginia 23606, USA*
[5]*Departament d'Estructura i Constituents de la Matèria, Institut de Ciències del Cosmos (ICC), Universitat de Barcelona, Martí Franquès 1, E08028-Spain*
[6]*Department of Physics, The City College of New York, New York, New York 10031, USA*
[7]*Graduate School and University Center, The City University of New York, New York, New York 10016, USA*
[8]*RIKEN BNL Research Center, Brookhaven National Laboratory, Upton, New York 11973, USA*
[9]*Department of Physics, University of Washington, Box 351560, Seattle, Washington 98195, USA*
(Received 14 August 2015; published 9 December 2015)

Lattice QCD with background magnetic fields is used to calculate the magnetic moments and magnetic polarizabilities of the nucleons and of light nuclei with $A \leq 4$, along with the cross section for the $M1$ transition $np \to d\gamma$, at the flavor SU(3)-symmetric point where the pion mass is $m_\pi \sim 806$ MeV. These magnetic properties are extracted from nucleon and nuclear energies in six uniform magnetic fields of varying strengths. The magnetic moments are presented in a recent article [S. Beane *et al.*, Phys. Rev. Lett. 113, 252001 (2014)]. For the charged states, the extraction of the polarizability requires careful treatment of Landau levels, which enter nontrivially in the method that is employed. The nucleon polarizabilities are found to be of similar magnitude to their physical values, with $\beta_p = 5.22(^{+0.66}_{-0.45})(0.23) \times 10^{-4}$ fm^3 and $\beta_n = 1.253(^{+0.056}_{-0.067})(0.055) \times 10^{-4}$ fm^3, exhibiting a significant isovector component. The dineutron is bound at these heavy quark masses, and its magnetic polarizability, $\beta_{nn} = 1.872(^{+0.121}_{-0.113})(0.082) \times 10^{-4}$ fm^3, differs significantly from twice that of the neutron. A linear combination of deuteron scalar and tensor polarizabilities is determined by the energies of the $j_z = \pm 1$ deuteron states and is found to be $\beta_{d,\pm 1} = 4.4(^{+1.6}_{-1.5})(0.2) \times 10^{-4}$ fm^3. The magnetic polarizabilities of the three-nucleon and four-nucleon systems are found to be positive and similar in size to those of the proton, $\beta_{^3\mathrm{He}} = 5.4(^{+2.2}_{-2.1})(0.2) \times 10^{-4}$ fm^3, $\beta_{^3H} = 2.6(1.7)(0.1) \times 10^{-4}$ fm^3, and $\beta_{^4\mathrm{He}} = 3.4(^{+2.0}_{-1.9})(0.2) \times 10^{-4}$ fm^3. Mixing between the $j_z = 0$ deuteron state and the spin-singlet np state induced by the background magnetic field is used to extract the short-distance two-nucleon counterterm, $\bar{L}_1$, of the pionless effective theory for NN systems (equivalent to the meson-exchange current contribution in nuclear potential models) that dictates the cross section for the $np \to d\gamma$ process near threshold. Combined with previous determinations of NN scattering parameters, this enables an *ab initio* determination of the threshold cross section at these unphysical masses.

DOI: 10.1103/PhysRevD.92.114502 PACS numbers: 11.15.Ha, 12.38.Gc, 13.40.Gp

I. INTRODUCTION

The charge, magnetic moment, and magnetic polarizability of a composite system describe its linear and quadratic response to a uniform, time-independent magnetic field. These properties are determined by the distribution of the constituents of the system and by the currents induced by the field. As such, measurements of the magnetic properties of the nucleons and nuclei provide important information about their internal structure. Furthermore, these quantities also serve to parametrize the cross section for low-energy Compton scattering on such targets. Historically, the magnetic moments of nucleons and light nuclei provided some of the first indications of substructure, and by now they are well known. The primary focus of this article is the magnetic polarizabilities and the cross section for the radiative capture process $np \to d\gamma$ at low energies which is

dominated by the $M1$ multipole. While the magnetic polarizability of the proton,[1] $\beta_p^{\rm exp} = (3.15 \pm 0.35 \pm 0.20 \pm 0.30) \times 10^{-4}$ fm^3, is well determined experimentally [2–7], the magnetic polarizability of the neutron $\beta_n^{\rm exp} = (3.65 \pm 1.25 \pm 0.20 \pm 0.80) \times 10^{-4}$ fm^3 remains quite uncertain [5,6,8–10]. This uncertainty is largely a consequence of the lack of a free neutron target; the neutron polarizability must be determined from that of light nuclei, primarily the deuteron (see Ref. [10] for a recent summary). The smallness of the nucleon polarizabilities, compared with their spatial volumes, ~ 1 fm^3, indicates that they are quite magnetically rigid, with the spins and currents of their constituents influenced only at a modest level by external fields. The uncertainty in $\beta_n^{\rm exp}$ is large enough so that a significant isovector polarizability remains a possibility. For a recent review, see Ref. [11].

From a theoretical standpoint, the leading contributions to the nucleon magnetic polarizabilities result from both pion-loop effects and Δ-resonance pole contributions [11–17]. The Δ-pole contribution is $\mathcal{O}(e^2/[M_N^2(M_\Delta - M_N)])$ and is considerably larger than the experimentally determined polarizabilities. At the physical light-quark masses, significant cancellations between the paramagnetic (Δ-pole) and diamagnetic (loop) contributions are in effect. As the various contributions depend differently on the light-quark masses (the leading pion-loop contributions scale as $\sim m_\pi^{-1}$ while the Δ-pole contribution is only weakly dependent on the quark masses), it is expected that β_p and β_n will vary reasonably rapidly near the physical point.[2] Because it is relatively mass independent, the Δ-pole contribution provides an estimate of the expected size for polarizabilities at any quark mass, and it will be used to assess the naturalness of the polarizabilities extracted from the present lattice QCD (LQCD) calculations.

The leading contributions to the magnetic polarizabilities of light nuclei are determined by the nucleon charges, magnetic moments, and polarizabilities. At a subleading level, the forces between nucleons, both those responsible for nuclear binding and meson-exchange currents (MECs), modify these one-body contributions and produce short-distance contributions that are unrelated to the electromagnetic interactions of single nucleons. Accounting for this in a consistent manner is nontrivial and requires a well-controlled power counting. This has been investigated in detail for the deuteron [19] and light nuclei [20]. Experimentally, the polarizabilities of the deuteron have been measured through Compton scattering (leading to extractions of the neutron magnetic polarizability), and further measurements will be performed with increased precision at the HIγS facility [21], at MAX-Lab at Lund [22], and at MAMI in Mainz [23]. Plans for a new generation of Compton scattering experiments on other light nuclei are also being developed (see, for example, Refs. [24–26]).

The radiative capture process, $np \to d\gamma$, and the inverse processes of deuteron electro- and photodisintegration, $\gamma^{(*)} d \to np$, are important in early universe cosmology and have led to critical insights into the interactions between nucleons and, in particular, interactions with photons. At very low energies, the $M1$ magnetic multipole transition amplitude is dominant and is determined primarily by the isovector nucleon magnetic moment. The short distance contributions (equivalently, MECs) are subleading, modify the cross sections at $\mathcal{O}(10\%)$ [27,28], and are well determined by experiment in this particular case. Given the phenomenological importance of this and other related processes, it is important to understand these contributions from first principles.

In this work, we present LQCD calculations of the magnetic moments and polarizabilities of the proton, neutron, and s-shell nuclei up to atomic number $A = 4$. Further, the $j_z = I_z = 0$ np systems are used to investigate the short-distance two-nucleon contributions to the cross section for $np \to d\gamma$. The methods and calculations that are presented are an extension of those used to calculate the magnetic moments of light nuclei in Ref. [29], and the results for the capture cross section have been recently highlighted in Ref. [30]. In Sec. II, the methodology of using background magnetic fields in LQCD calculations to determine hadron magnetic moments and polarizabilities and magnetic transition amplitudes is presented. Section III discusses the results of our calculations, by first discussing the general analysis methods used to extract the magnetic properties from energy shifts before turning to a discussion of each of the nucleons and nuclei that are studied. Our results are summarized in Sec. IV, and opportunities for possible extensions of this work are also outlined. Finally, Appendix A is dedicated to defining the formalism underpinning the LQCD methodology used in the present calculations. Explicit examples centered on the behavior of pointlike charged particles are explored.

II. METHODOLOGY

To calculate the magnetic structure of nucleons and light nuclei, and the low-energy cross section for $np \to d\gamma$, it is sufficient to perform LQCD calculations of these systems in uniform time-independent magnetic fields. In sufficiently weak background fields, the quantities of interest can be extracted directly from the energy eigenvalues of the spin states of these systems.

[1]The experimental polarizability reported here is defined with Born terms subtracted; the total $\mathcal{O}(B^2)$ shift in the energy of the proton is larger by $(16\pi M^3)^{-1} = 0.15 \times 10^{-4}$ fm^3 [1].

[2]Recent chiral effective field theory calculations support this expectation [17], and the expectations are not substantially altered in the case of partially quenched chiral perturbation theory [18].

A. Background magnetic fields

In this work, lattice QCD calculations are performed using one ensemble of QCD gauge-field configurations with $N_f = 3$ degenerate dynamical flavors of light quarks on a $L^3 \times T = (32^3 \times 48)a^4$ discretized spacetime. This ensemble was generated using a Lüscher-Weisz gauge action [31] and a tadpole-improved clover-fermion action [32] at a coupling corresponding to a lattice spacing of $a = 0.110(1)$ fm [33] (further details of this ensemble can be found in Refs. [34,35]). All three light-quark masses in this ensemble are equal to that of the physical strange quark, producing a pion of mass $m_\pi \sim 806$ MeV. In the present set of calculations, $\mathcal{O}(10^3)$ gauge-field configurations separated by 10 hybrid Monte Carlo trajectories were used from this ensemble.

Background electromagnetic fields have been used extensively in previous calculations of the electromagnetic properties of single hadrons, such as the magnetic moments of the lowest-lying baryons [18,29,36–43], the polarizabilities of mesons [39,41,44–46], and the electric polarizabilities of baryons [46,47]. In addition, the magnetic moments of light nuclei have recently been calculated in Ref. [29]. For the quark fields, with electric charges q_q ($q_u = +\frac{2}{3}$ and $q_{d,s} = -\frac{1}{3}$ for the up, down, and strange quarks, respectively), to encounter uniform magnetic flux throughout the lattice, the field strength is quantized according to the condition [48]

$$e\mathbf{B} = \frac{6\pi}{L^2}\tilde{n}\mathbf{e_z}, \quad \tilde{n} \in \mathbb{Z}, \tag{1}$$

where e is the magnitude of the electron charge and we consider explicitly fields in the $x_3 \equiv z$ direction as indicated by the unit vector $\mathbf{e_z}$. Neglecting the electric charges of the sea quarks, a quantized, time-independent, and uniform background magnetic field oriented in the positive x_3 direction can be implemented by multiplying the QCD gauge link variables by $U_Q(1)$ link fields, $U_\mu^{(Q)}(x)$, of the form

$$\begin{aligned} U_1^{(Q)}(x) &= \begin{cases} 1 & \text{for } x_1 \neq L-a \\ \exp\left[-iq_q\tilde{n}\frac{6\pi x_2}{L}\right] & \text{for } x_1 = L-a \end{cases}, \\ U_2^{(Q)}(x) &= \exp\left[iq_q\tilde{n}\frac{6\pi a x_1}{L^2}\right], \\ U_3^{(Q)}(x) &= 1, \\ U_4^{(Q)}(x) &= 1, \end{aligned} \tag{2}$$

where $\tilde{n}$ is an integer satisfying $|\tilde{n}| \leq \frac{1}{4}L^2/a^2$ (in Euclidean space, x_4 corresponds to the Wick-rotated time coordinate). In physical units, the background magnetic fields used in this work are quantized in units of $e\mathbf{B} \sim 0.059\tilde{n}$ GeV$^2\mathbf{e_z}$; in comparison to the nucleon mass, the dimensionless ratio $e|\mathbf{B}|/M_N^2 \sim 0.013$ for the smallest field suggesting the deformations arising from the magnetic field are perturbatively small compared to QCD effects for $|\tilde{n}| \lesssim 10$. As $m_u = m_d = m_s$ in these calculations, the up-quark propagator in the $\tilde{n} = 1$ field is the same as the down- or strange-quark propagator in the $\tilde{n} = -2$ field, with similar relations for the other magnetic field strengths. To optimize the reuse of light-quark propagators in the calculation, different quark electric charges were implemented by using a different magnetic field (with the same charge). Consequently, the $U_Q(1)$ fields that are used in this work correspond to $\tilde{n} = 0, +1, -2, +3, +4, -6, +12$, corresponding to magnetic fields of $e\mathbf{B} \sim 0, 0.06, -0.12, 0.18, 0.24, -0.36, 0.71$ GeV$^2\mathbf{e_z}$, respectively.

In the presence of a time-independent and uniform magnetic field, the energy eigenstates of a structureless charged particle with definite angular momentum along the field direction are described by Landau levels and plane waves, rather than by three-momentum plane waves alone. One of the subtle finite-volume (FV) effects introduced into this calculation is the loss of translational invariance in the interaction of charged particles with the background gauge field. We give a brief description of this problem and relegate the more technical aspects of the discussion to Appendix A. For the implementation of the magnetic field using the links in Eq. (2), the lack of translational invariance is made obvious by the Wilson loops,

$$\begin{aligned} W_1(x_2) &= \prod_{j=0}^{L/a-1} U_1^{(Q)}(x + ja\hat{x}_1) = \exp\left[-iq_q\tilde{n}\frac{6\pi x_2}{L}\right], \\ W_2(x_1) &= \prod_{j=0}^{L/a-1} U_2^{(Q)}(x + ja\hat{x}_2) = \exp\left[iq_q\tilde{n}\frac{6\pi x_1}{L}\right], \end{aligned} \tag{3}$$

which wrap around the x_1 and x_2 directions of the lattice geometry, respectively. These exhibit explicit spatial dependence. Further, there are additional effects for charged-particle correlation functions arising from their gauge dependence.

Because of the lack of translational invariance, the links employed in Eq. (2) define a spatial origin $\mathbf{x} = \mathbf{0}$, where the gauge potential vanishes, $\mathbf{A}(\mathbf{x}) = \mathbf{0}$. In performing the present calculations, the source points for the correlation functions are not restricted to $\mathbf{x} = \mathbf{0}$ but instead are randomly distributed within the lattice volume, which approximately restores translational invariance. In the case of charged-particle correlation functions, this averaging leads to nontrivial effects, because the overlap of a given hadronic operator onto the various Landau levels depends on the source location. This is explicated in Appendix A, where additional methods of restoring translational invariance are discussed in the context of a structureless charged particle.

Postmultiplication of $U_Q(1)$ links onto the QCD gauge links omits the effects of the external magnetic field on the

gluonic degrees of freedom through the fermion determinant. The present calculations therefore correspond to a partially quenched theory in which the sea quark charges are set to zero while the valence quark charges assume their physical values [18,49–51]. For a SU(3) symmetric choice of quark masses, as used herein, this does not affect the magnetic moments or the $np \to d\gamma$ transition (linear responses to the field) because the $N_f = 3$ charge matrix is traceless [18,29] and couplings to sea quarks explicitly cancel at this order [indeed the isovector nature of the $np \to d\gamma$ transition make it insensitive to disconnected contributions even away from the SU(3) symmetric point]. However, the magnetic polarizabilities receive contributions from terms in which the two photons associated with the magnetic field interact with zero, one, or two sea quark loops. The terms involving zero and two sea quark loops are correctly implemented; however, the square of the light-quark electric-charge matrix is not traceless and terms involving the two photons interacting with one sea quark loop will contribute to isoscalar quantities for any nonzero charge matrix. In the present work, these terms are omitted for computational expediency.[3] Generally, it has been found that the related disconnected contributions to analogous single-hadron observables are small for the vector current [52,53], and we expect that this behavior persists in nuclei. It is important to remember that this systematic ambiguity is restricted to the case of the isoscalar polarizabilities, and that the isovector and isotensor combinations, such as $\beta_p - \beta_n$, will be correctly calculated for the SU(3) symmetric case.

B. Interpolating operators and contractions

To probe the energy eigenstates of the systems under consideration, interpolating operators are constructed with the desired quantum numbers. In principle, any choice of operator that has an overlap onto a given eigenstate is acceptable. However, poor choices will have small overlaps onto the state of interest and hence will give rise to "noisy" signals with significant contamination from other states with the same quantum numbers. For a vanishing background magnetic field, the energy eigenstates are also momentum eigenstates, and to access the ground state energy, it is simplest to choose interpolating operators that project onto states with zero three-momentum. In this work, this approach is followed for both the neutron and the proton (despite the proton carrying a positive electric charge). The proton correlation functions are of the form

$$C_p^{(P,S)}(t;\mathbf{x}_i) = \langle 0|\tilde{\mathcal{O}}_p^{(P,S)}(t;\mathbf{0})\bar{\mathcal{O}}_p^{(S)}(\mathbf{x}_i,0)|0\rangle_{\mathbf{B}}, \qquad (4)$$

with interpolating operators that are given by

$$\begin{aligned}
\mathcal{O}_p^{(S)}(\mathbf{x},t) &= \epsilon^{ijk}[\tilde{u}_+^i(\mathbf{x},t)C\gamma_5\tilde{d}_+^j(\mathbf{x},t)]\tilde{u}_+^k(\mathbf{x},t),\\
\tilde{\mathcal{O}}_p^{(P)}(t;\mathbf{p}) &= \sum_{\mathbf{x}} e^{i\mathbf{p}\cdot\mathbf{x}}\epsilon^{ijk}[u_+^i(\mathbf{x},t)C\gamma_5 d_+^j(\mathbf{x},t)]u_+^k(\mathbf{x},t),\\
\tilde{\mathcal{O}}_p^{(S)}(t;\mathbf{p}) &= \sum_{\mathbf{x}} e^{i\mathbf{p}\cdot\mathbf{x}}\epsilon^{ijk}[\tilde{u}_+^i(\mathbf{x},t)C\gamma_5\tilde{d}_+^j(\mathbf{x},t)]\tilde{u}_+^k(\mathbf{x},t)\\
&= \sum_{\mathbf{x}} e^{i\mathbf{p}\cdot\mathbf{x}}\mathcal{O}_p^{(S)}(\mathbf{x},t), \qquad (5)
\end{aligned}$$

where $\langle\cdots\rangle_{\mathbf{B}}$ indicates ensemble averaging with respect to QCD in the presence of the $U_Q(1)$ links corresponding to a uniform background magnetic field $\mathbf{B} = B\mathbf{e_z}$, and where the spin indices of the operators, carried by the third quark, are suppressed. In Eq. (5), $\tilde{q}(x)$ corresponds to a quark field of flavor $q = u, d$ that has been smeared [54] in the spatial directions using a Gaussian form, while $q(x)$ corresponds to a local field. Additionally, the subscript $_+$ on the quark fields implies that they are explicitly projected onto positive energy modes, that is, $u_+^i(\mathbf{x},t) = (1+\gamma_4)u^i(\mathbf{x},t)$. The superscript (P,S) on an interpolating operator (and hence the correlation function) indicates a point or smeared form, respectively, $C = i\gamma_4\gamma_2$ is the charge conjugation matrix, and $\bar{\mathcal{O}}_p^{(S)} = \mathcal{O}_p^{(S)\dagger}\gamma_4$. Neutron correlation functions are constructed from those of the proton by interchanging $u \leftrightarrow d$. The correlation functions with the quantum numbers of nuclei, constructed using the methods discussed in detail in Refs. [34,55], are built recursively using sink-projected nucleon "blocks" that involve either smeared or local fields. For the present calculations, zero momentum states are built from zero momentum blocks, although more complicated constructions can also be considered.

As suggested in Ref. [56], in order to study the proton in a magnetic field, it would be more appropriate to use interpolating operators that project onto the lowest-lying Landau level, rather than projecting onto three-momentum plane waves. This would enhance the overlap of the interpolating operator onto the lowest, close-to-Landau energy eigenstate and suppress the overlap onto higher states. However, it is unclear how to generalize such a framework to nuclei constructed from nucleon blocks. While single-hadron blocks provide a good basis for the construction of correlation functions of nuclei in the absence of background fields, this will not necessarily be the case in a magnetic field. The problem is exemplified by ^{3}He, a $j = \frac{1}{2}$ nucleus composed of two protons and a neutron. Assuming a compact state (which it has been shown to be at the quark masses used in this work through calculations in multiple lattice volumes [34]), the wave function of the nucleus is a Landau level determined by its electric charge of $Q = 2e$, while that of the proton is a Landau level determined by $Q = e$, and that of the neutron is a momentum eigenstate. Proton blocks could be constructed by projection onto a given Landau level at the sink, leading to presumably improved signals for the proton correlation functions. However, combining Landau-projected proton blocks and

[3]Several approaches to these terms have been considered recently [46,47] and may be investigated in future studies of nuclei, although significant computational resources are required.

momentum-projected neutron blocks will not necessarily produce interpolating operators that couple well to the ^{3}He Landau levels. For larger nuclei, this problem becomes even more severe. There are interesting directions that could be pursued in this regard, for example, constructing single hadron blocks that are projected onto the Landau levels of the "target" nucleus. However, *a priori* it is difficult to ascertain how efficacious such approaches will be. In the current work the same interpolating operators used for zero-field calculations are used for calculations in the presence of background magnetic fields. Although these are not ideal interpolating operators, they are not orthogonal to the expected eigenstates, and the results extracted from this naive approach serve as a benchmark for more sophisticated methods that can be explored in future investigations.

The correlation functions investigated in this work with the quantum numbers of nuclei are of the form

$$C_{h;j_z}(t;\mathbf{B}) = \langle 0|\tilde{f}_{h;j_z}[\tilde{\mathcal{O}}^{(S,P)}_{p,n}(t;\mathbf{0})]f_{h;j_z}[\bar{\mathcal{O}}^{(S)}_{p,n}(t;\mathbf{x}_i)]|0\rangle_{\mathbf{B}}. \quad (6)$$

The exact source and sink interpolating functions, $f_{h;j_z}$ and $\tilde{f}_{h;j_z}$, depend on the quantum numbers of the nucleus and are defined implicitly through the recursive procedures of Ref. [55]. For nuclei with nonzero total spin j, the z component of spin, j_z, is made explicit as each magnetic substate is studied individually. On each QCD gauge configuration, up- and down-quark propagators are generated for each of the seven magnetic field strengths from 48 uniformly distributed Gaussian-smeared sources. The position of the first source was randomly chosen and the remaining sources were placed on a regular, three-dimensional grid relative to that location. The source locations were selected after the background magnetic field was applied, and hence there was no correlation between the source location and the position of the zero of the vector potential. As the calculations from the different source locations on each gauge field are averaged over, the dependence of $C_{h;j_z}(t;\mathbf{B})$ on the source location $\mathbf{x}_i$ is suppressed. This location averaging effectively projects the source interpolating operator onto zero momentum and is discussed in detail in Appendix A. In most cases, two correlation functions are constructed for each nuclear state using the smeared and point sink interpolators, although for larger nuclei there are more possibilities than are calculated.

C. Magnetic field strength dependence of energies

In a uniform background magnetic field, the energy eigenvalues of a hadron, h, either a nucleon or a nucleus, with spin $j \le 1$ polarized in the z direction, with magnetic quantum number j_z, are of the form

$$E_{h;j_z}(\mathbf{B}) = \sqrt{M_h^2 + P_\parallel^2 + (2n_L+1)|Q_h e\mathbf{B}|} - \boldsymbol{\mu}_h\cdot\mathbf{B} - 2\pi\beta_h^{(M0)}|\mathbf{B}|^2 - 2\pi\beta_h^{(M2)}\langle\hat{T}_{ij}B_iB_j\rangle + \cdots, \quad (7)$$

where M_h is the mass of the hadron, $P_\parallel$ is its momentum parallel to the magnetic field, Q_h is its charge in units of e, and n_L is the quantum number of the Landau level that it occupies. For a nucleon or nucleus with spin $j \ge \frac{1}{2}$, there is a contribution from the magnetic moment, $\boldsymbol{\mu}_h$, that is linear in the magnetic field. The magnetic polarizability is conveniently decomposed into multipoles, with $\beta_h \equiv \beta_h^{(M0)}$ denoting the scalar polarizability and $\beta_h^{(M2)}$ denoting the tensor polarizability (the latter contributes for hadrons with $j \ge 1$). $\hat{T}_{ij}$ is a traceless symmetric tensor operator which, when written in terms of angular momentum generators, is of the form

$$\hat{T}_{ij} = \frac{1}{2}\left[\hat{J}_i\hat{J}_j + \hat{J}_j\hat{J}_i - \frac{2}{3}\delta_{ij}\hat{J}^2\right], \quad (8)$$

and $\langle\cdots\rangle$ in Eq. (7) denotes its expectation value.[4] Note that the polarizabilities defined here represent the full quadratic response to the field and differ from other conventions used in the literature where Born terms are explicitly removed (for a discussion, see, e.g., Ref. [57]). The ellipses denote contributions that involve three or more powers of the magnetic field. The spin-averaged energy eigenvalues project onto the scalar contributions,

$$\langle E_h(\mathbf{B})\rangle \equiv \frac{1}{2j+1}\sum_{j_z=-j}^{j} E_{h;j_z}(\mathbf{B}) = \sqrt{M_h^2 + P_\parallel^2 + (2n_L+1)|Q_h e\mathbf{B}|} - 2\pi\beta_h^{(M0)}|\mathbf{B}|^2 + \cdots, \quad (9)$$

where the ellipses denote contributions of $\mathcal{O}(|\mathbf{B}|^4)$ and higher. For spin-j states, the energy difference between $j_z = \pm j$ isolates the magnetic moment at lowest order in the expansion. Other combinations of the energy eigenvalues of the individual spin components can be formed to isolate higher multipoles.

III. RESULTS

A. Extraction of energy levels

With the background magnetic field given in Eq. (2), well-defined energy levels exist for each value of the magnetic field strength. To determine the magnetic polarizabilities, energy eigenvalues are determined from the appropriate correlation functions, the $C_{h;j_z}(t;\mathbf{B})$ defined in Eq. (6). The individual correlation functions associated

[4]For a magnetic field aligned in the z direction, it follows that $\langle\hat{T}_{ij}B_iB_j\rangle = \langle\hat{T}_{zz}B^2\rangle = (j_z^2 - \frac{1}{3}j(j+1))B^2$. This vanishes for both the $j=0$ and $j=\frac{1}{2}$ states, and takes the values $\langle\hat{T}_{ij}B_iB_j\rangle = \frac{1}{3}B^2$ for $j=1$, $j_z=\pm1$ states and $\langle\hat{T}_{ij}B_iB_j\rangle = -\frac{2}{3}B^2$ for $j=1$, $j_z=0$ states.

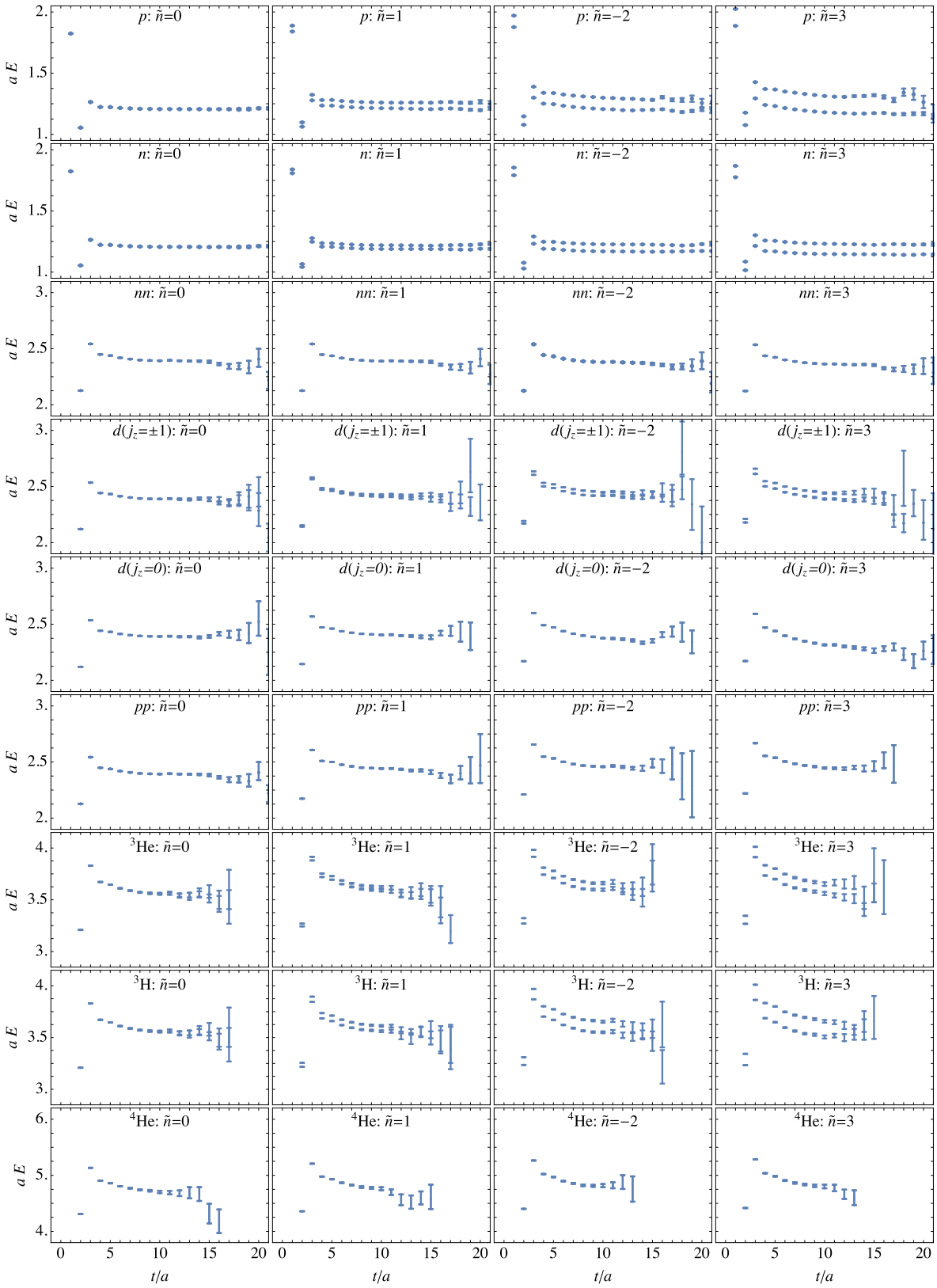

FIG. 1 (color online). EMPs obtained from the smeared-smeared nucleon and nuclear correlation functions for the lowest-four magnetic field strengths. The $j_z = \pm j$ states are shown for each hadron.

with each state in each magnetic field are examined, and the time intervals over which they are consistent with single exponential behavior are determined. Effective mass plots (EMPs) associated with representative correlation functions obtained in the magnetic fields with $\tilde{n} = 0, 1, -2, 3$ are shown in Fig. 1. Having identified these time intervals, the main analysis focuses on ratios of these correlation functions constructed as

$$R_{h;j_z}(t;\mathbf{B}) = \frac{C_{h;j_z}(t;\mathbf{B})}{C_{h;j_z}(t;\mathbf{B}=0)} \overset{t\longrightarrow\infty}{\longrightarrow} Z_{h;j_z}(\mathbf{B}) e^{-\delta E_{h;j_z}(\mathbf{B})t}, \quad (10)$$

where $\delta E_{h;j_z}(\mathbf{B}) = E_{h;j_z}(\mathbf{B}) - E_{h;j_z}(\mathbf{0})$ is the energy difference induced by the magnetic field, and $Z_{h;j_z}(\mathbf{B})$ is a time-independent, but field-dependent, overlap factor. To be specific, $h = p$, n, nn, d, pp, ^{3}He, ^{3}H, and ^{4}He are considered in all magnetic substates. It is advantageous to work with ratios of correlation functions because fluctuations present in the energies extracted from individual correlation functions cancel to a significant degree in the ratio.[5] The energy shifts are extracted from these ratios in the time regions in which the contributing individual correlation functions show single state dominance by either directly fitting the ratio or, alternatively, by fitting the effective mass resulting from the double ratio

$$\delta E_{h;j_z}(\mathbf{B};t,t_J) = \frac{1}{t_J}\log\left(\frac{R_{h;j_z}(t;\mathbf{B})}{R_{h;j_z}(t+t_J;\mathbf{B})}\right) \overset{t\longrightarrow\infty}{\longrightarrow} \delta E_{h;j_z}(\mathbf{B}), \quad (11)$$

where t_J represents a temporal offset that can be chosen to optimize energy extractions. The fits are performed using the correlated χ^2-minimization procedure, with the covariance matrix determined using jackknife or bootstrap resampling. A systematic fitting uncertainty is estimated by performing fits over multiple fitting intervals within the region of single-exponential dominance for a given system. The primary analysis in this work is based on fitting the ratios of correlation functions obtained from binning source-averaged measurements into $N_b = 100$ blocked samples and generating $N_B = 200$ bootstrap samples from these blocked samples. Alternate analyses are also undertaken in which differences include varying the statistical procedures and also performing constant fits to effective mass functions formed from different values of t_J and other possible variations. Consistent results are obtained.

To extract the magnetic polarizabilities, ratios of the correlation functions associated with the maximally stretched spin states can be formed such that the leading magnetic-moment contributions cancel,

$$\bar{R}_h(t;\mathbf{B}) = \frac{C_{h;j_z=j}(t;\mathbf{B})}{C_{h;j_z=j}(t;\mathbf{0})}\frac{C_{h;j_z=-j}(t;\mathbf{B})}{C_{h;j_z=-j}(t;\mathbf{0})} \to \tilde{Z}e^{-2\delta\langle E_h(\mathbf{B})\rangle t}, \quad (12)$$

where $\delta\langle E_h(\mathbf{B})\rangle = \langle E_h(\mathbf{B})\rangle - M_h$ is the spin-averaged energy shift. Similarly, the spin difference between maximal $j_z = \pm j$ states eliminates the spin-independent terms, leaving only the magnetic-moment contribution and $\mathcal{O}(|\mathbf{B}|^3)$ and higher terms. This has been used to extract magnetic moments in Refs. [29,43] using the ratio

$$\Delta R_h(t;\mathbf{B}) = \frac{C_{h;j_z=j}(t;\mathbf{B})}{C_{h;j_z=j}(t;\mathbf{0})}\frac{C_{h;j_z=-j}(t;\mathbf{0})}{C_{h;j_z=-j}(t;\mathbf{B})} \to \Delta\tilde{Z}e^{-(E_{h;j}(\mathbf{B})-E_{h;-j}(\mathbf{B}))t}. \quad (13)$$

In the present work, the individual spin states are used to extract the magnetic moments and polarizabilities in a coupled fit as the latter quantities are the primary target of this study. However, the magnetic moments have also been extracted from the spin-difference ratios, Eq. (13) [29], and that approach is found to lead to consistent but more precise results and remains the preferred method for extracting the magnetic moments. Given the more complicated nature of the fits we perform here in order to obtain sensitivity to the polarizabilities, it is unsurprising that the uncertainties on the lower order terms are larger. In what follows, we present the magnetic moments that result from the coupled fits for completeness, but use the previous fits to spin-difference ratios as the best estimates of these quantities.

Figures 2 and 3 show the ratios of correlation functions used in the extraction of energy shifts for each magnetic field strength and spin component. Results from all six nonzero magnetic field strengths are shown. In each case, the associated single exponential fit to the ratio of correlation functions is shown, along with the associated statistical uncertainty. Fits over all time ranges in $[t_{\rm min}, t_{\rm max}]$ are considered, where $t_{\rm max} = 24$ and $t_{\rm min}$ is set by requiring consistency with single exponential behavior of the individual correlators that form a given ratio. The central fit is identified as that over the time range with $t_{\rm max} - t_{\rm min} > 3$ with the lowest correlated χ^2/d.o.f. The standard deviation of all fits over subsets of time ranges in the interval $[t_{\rm min} - 1, t_{\rm max}]$ that have a χ^2 within one unit of the minimum χ^2 ($\chi^2 \to \chi^2_{\rm min} + 1$) is taken as the fitting systematic uncertainty. The extracted energy shifts are tabulated in Table I.

The correlation functions associated with the nucleons and nuclei are highly correlated, and therefore differences between the energies of two given states can be more accurately determined than those of each state individually. Of particular interest is the difference between the magnetic properties of a nucleus and that of its constituent nucleons. To highlight these differences, further ratios are constructed,

[5]Note that such ratios are formed after averaging over an ensemble of measurements.

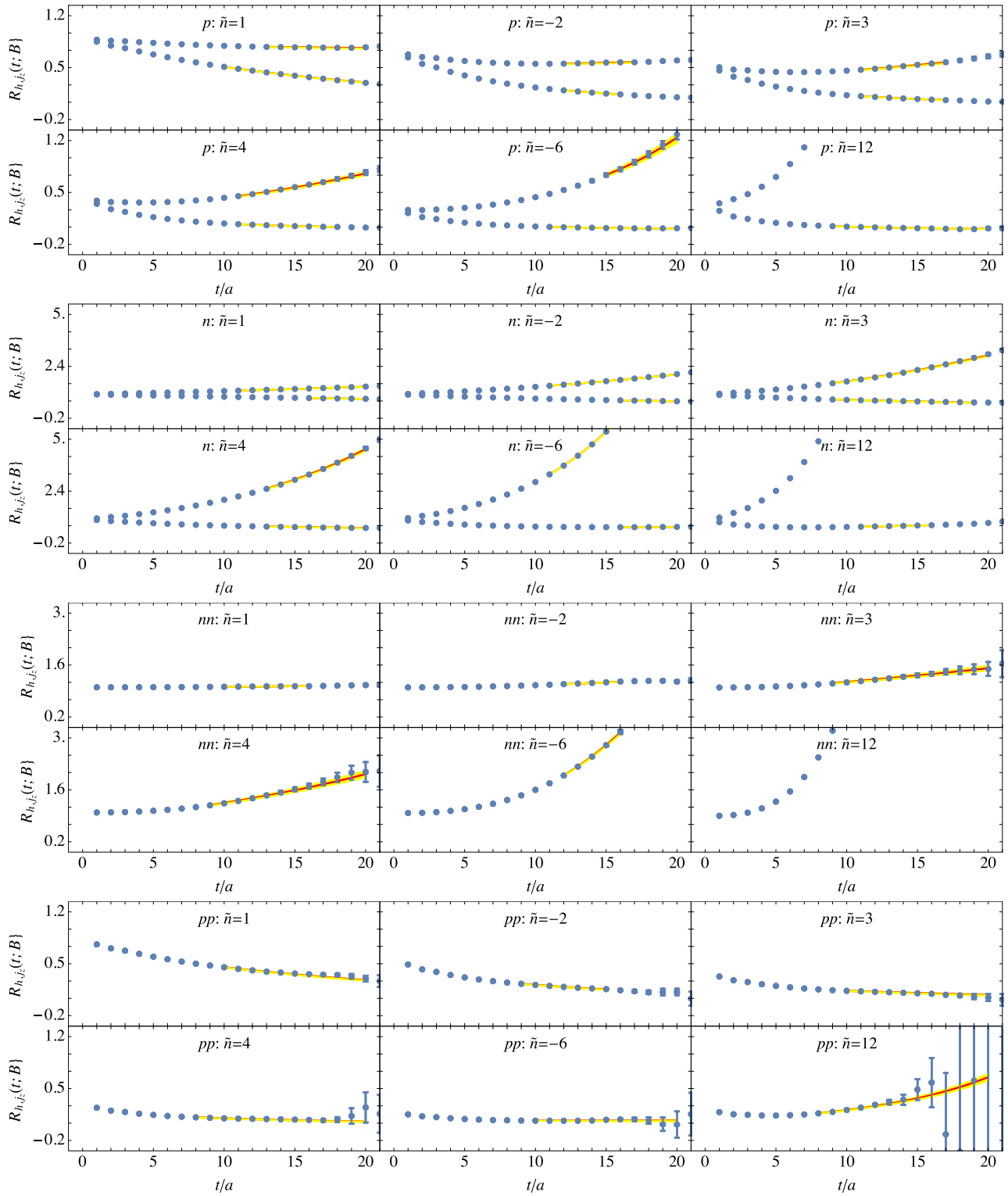

FIG. 2 (color online). The ratio of correlation functions associated with the p, n, nn, and pp systems. Results are shown for all six field strengths for the smeared-smeared correlators and for both $|j_z| = j$ states for states with $j > 0$. The shaded bands correspond to the statistical uncertainties of the given fit.

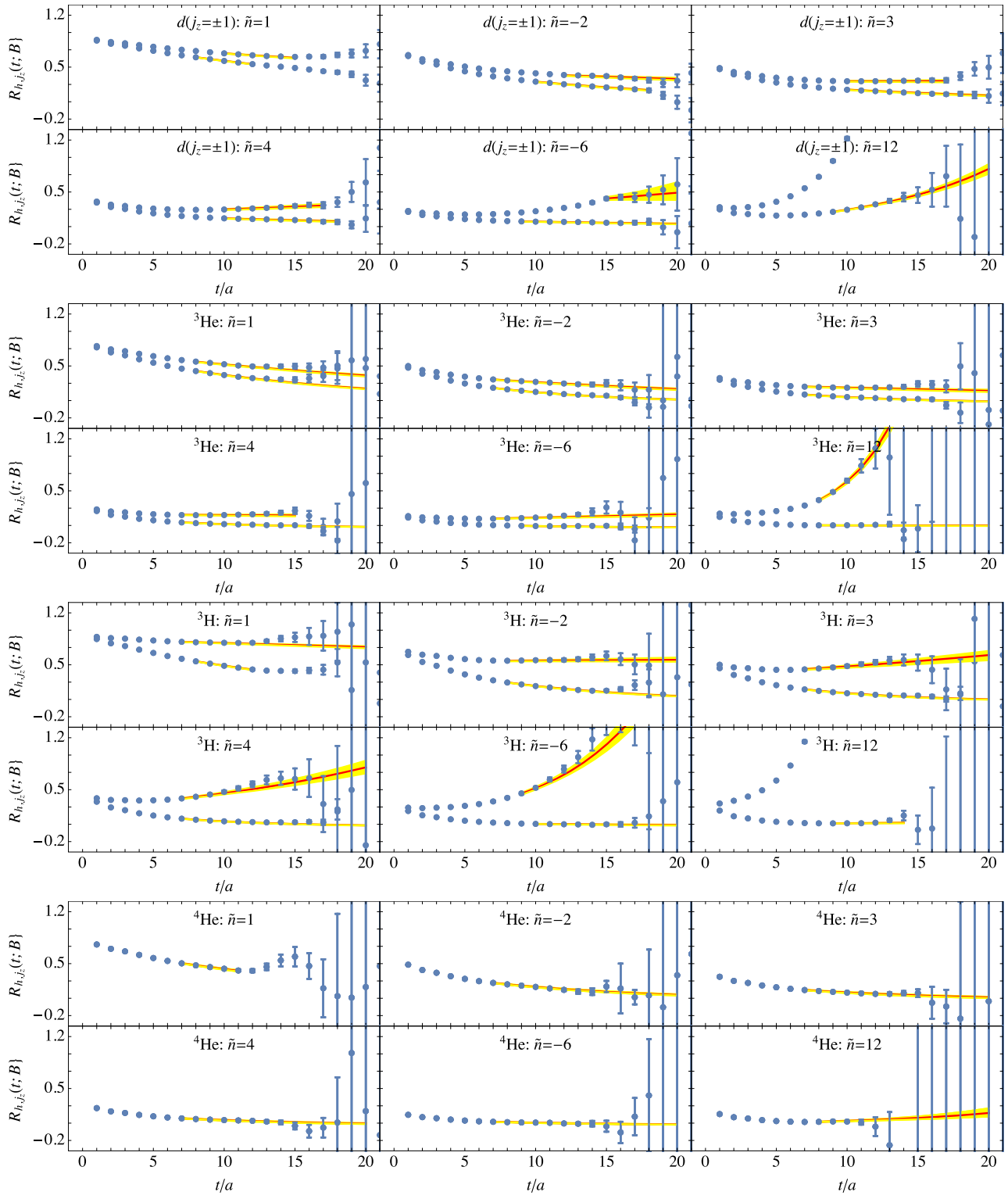

FIG. 3 (color online). The ratio of correlation functions associated with the d, ^{3}He, ^{3}H, and ^{4}He states. Results are shown for all six field strengths for the smeared-smeared correlators and for both $|j_z| = j$ states for states with $j > 0$. The shaded bands correspond to the statistical uncertainties of the given fit.

TABLE I. Extracted energy shifts of the nucleons and nuclei, where the first uncertainty is statistical and the second corresponds to the systematic uncertainty obtained from the variation of fitting ranges. The $j_z = 0$ deuteron state is studied separately.

State		$a\delta E_{h;j_z}(\tilde{n})$					
h	j_z	$\tilde{n}=1$	$\tilde{n}=-2$	$\tilde{n}=3$	$\tilde{n}=4$	$\tilde{n}=-6$	$\tilde{n}=12$
p	$\frac{1}{2}$	0.0032(11)(17)	0.0839(24)(0)	−0.0324(22)(19)	−0.0581(26)(12)	0.1288(51)(65)	−0.2495(17)(13)
p	$-\frac{1}{2}$	0.05372(63)(68)	−0.0073(16)(7)	0.1035(34)(23)	0.1087(37)(42)	−0.1045(57)(41)	0.142(4)(16)
n	$\frac{1}{2}$	0.01297(32)(19)	−0.03741(12)(8)	0.0249(12)(19)	0.0184(21)(12)	−0.12694(35)(27)	−0.02318(91)(64)
n	$-\frac{1}{2}$	−0.01711(7)(17)	0.01749(75)(46)	−0.0584(10)(11)	−0.0831(17)(6)	−0.0027(23)(24)	−0.24212(63)(25)
nn	0	−0.00321(15)(32)	−0.0146(8)(12)	−0.0285(31)(21)	−0.0488(32)(36)	−0.1147(24)(99)	−0.2793(27)(26)
d	1	0.0190(16)(74)	0.0588(34)(44)	−0.0009(54)(31)	−0.0262(72)(61)	0.033(7)(15)	−0.337(22)(19)
d	−1	0.0398(8)(33)	0.0169(59)(79)	0.0523(58)(62)	0.041(8)(13)	−0.039(47)(28)	−0.114(7)(20)
pp	0	0.0490(19)(82)	0.0679(36)(56)	0.0536(55)(88)	0.062(5)(12)	0.001(11)(34)	−0.114(5)(15)
^{3}He	$\frac{1}{2}$	0.067(3)(24)	0.0408(38)(53)	0.123(8)(10)	0.126(8)(22)	−0.028(7)(27)	0.01(1)(69)
^{3}He	$-\frac{1}{2}$	0.034(3)(16)	0.112(4)(13)	0.023(7)(16)	0.0045(85)(94)	0.112(15)(77)	−0.262(11)(89)
^{3}H	$\frac{1}{2}$	0.007(1)(16)	0.100(4)(19)	−0.027(7)(25)	−0.058(7)(39)	0.06(2)(11)	−0.31(8)(12)
^{3}H	$-\frac{1}{2}$	0.058(2)(27)	−0.0025(35)(67)	0.125(7)(29)	0.138(8)(38)	−0.152(11)(35)	−0.02(2)(70)
^{4}He	0	0.056(4)(69)	0.086(7)(30)	0.090(14)(35)	0.098(15)(74)	0.09(1)(11)	−0.10(3)(62)

$$\delta R_{\mathcal{A},j_z}(t;\mathbf{B}) = \frac{R_{\mathcal{A}}(t;\mathbf{B})}{\prod_{h\in\mathcal{A}} R_h(t;\mathbf{B})} \overset{t\longrightarrow\infty}{\longrightarrow} \delta Z_{\mathcal{A}}(\mathbf{B}) \exp\left[-\left(\delta E_{\mathcal{A}}(\mathbf{B}) - \sum_{h\in\mathcal{A}} \delta E_h(\mathbf{B})\right) t\right], \tag{14}$$

where the nucleus $\mathcal{A}$ contains a set of nucleons, h, and the spin indices have been suppressed for brevity. Figure 4 shows this ratio of correlation functions for the nn, $j_z = \pm 1$ deuteron, and pp systems.

As discussed previously, the momentum-projected interpolating operators are not expected to provide particularly good overlap onto the low-energy eigenstates of the proton and charged nuclei in magnetic fields, which are expected to more closely resemble Landau wave functions. Indeed, the interpolating operators are found to overlap most strongly with states *other* than the lowest Landau level, as will be discussed below and in detail in Appendix A. In Fig. 5, the ratio of overlap factors of the extracted state at nonzero and zero background field strengths are shown. For the neutral states, the overlap is only weakly dependent on the field strength, but for charged states, the overlap rapidly decreases with increasing magnetic field strength. This indicates that care must be taken in interpreting the extracted states. It does not mean that unrelated states (those that are not continuously related as a function of the magnetic field) are being extracted for different field strengths, but instead the overlap onto the given state is decreasing.[6]

[6]Similar effects have been seen in constructing multipion correlation functions from combinations of pion interpolating operators built with differing momenta. Exponentially smaller overlaps were observed, although a consistent energy could be extracted [58,59]. In background electric fields, the overlap factors of momentum projected interpolating operators were also seen to decrease significantly with the applied field strength [41,42].

B. The coupled $j_z = I_z = 0$ two-nucleon channel

The $j_z = I_z = 0$ channel is special in that the presence of the magnetic field breaks isospin symmetry through the charge matrix and also introduces explicit spin dependence to the low-energy effective Hamiltonian. Consequently, the background magnetic field couples the $j_z = 0$ deuteron and $I_z = 0$ dinucleon states, and a more complicated analysis is required to extract the essential physics. The energy eigenvalues of this system result from diagonalizing a 2×2 truncated Hamiltonian in the basis formed from the $^1S_0$ and the $^3S_1$ states.[7] For nonvanishing magnetic fields, the off-diagonal elements of this truncated Hamiltonian receive contributions from magnetic transitions between the $^3S_1$ and $^1S_0$ channels induced by the nucleon isovector magnetic moment and short-distance two-nucleon interactions with the magnetic field resulting from meson-exchange currents in the context of potential models or local two-nucleon current couplings in effective field theory (EFT). As the nucleon isovector magnetic moment is large, the energy splittings between these states are significant for the magnetic field strengths employed.

[7]For the small magnetic field strengths considered in this work, the gap to excitations is significant, and such excitations can be neglected. Additionally, because of the tensor interaction, the $j = 1$ state involves both S-wave and D-wave contributions. The $^3S_1$-$^3D_1$ coupled channels are truncated down to the $^3S_1$ channel because the deuteron and dineutron are close in energy in the absence of a magnetic field, and the deuteron is predominantly S-wave (at least at the physical pion mass). For a more detailed discussion of the deuteron in a FV, see Refs. [60,61].

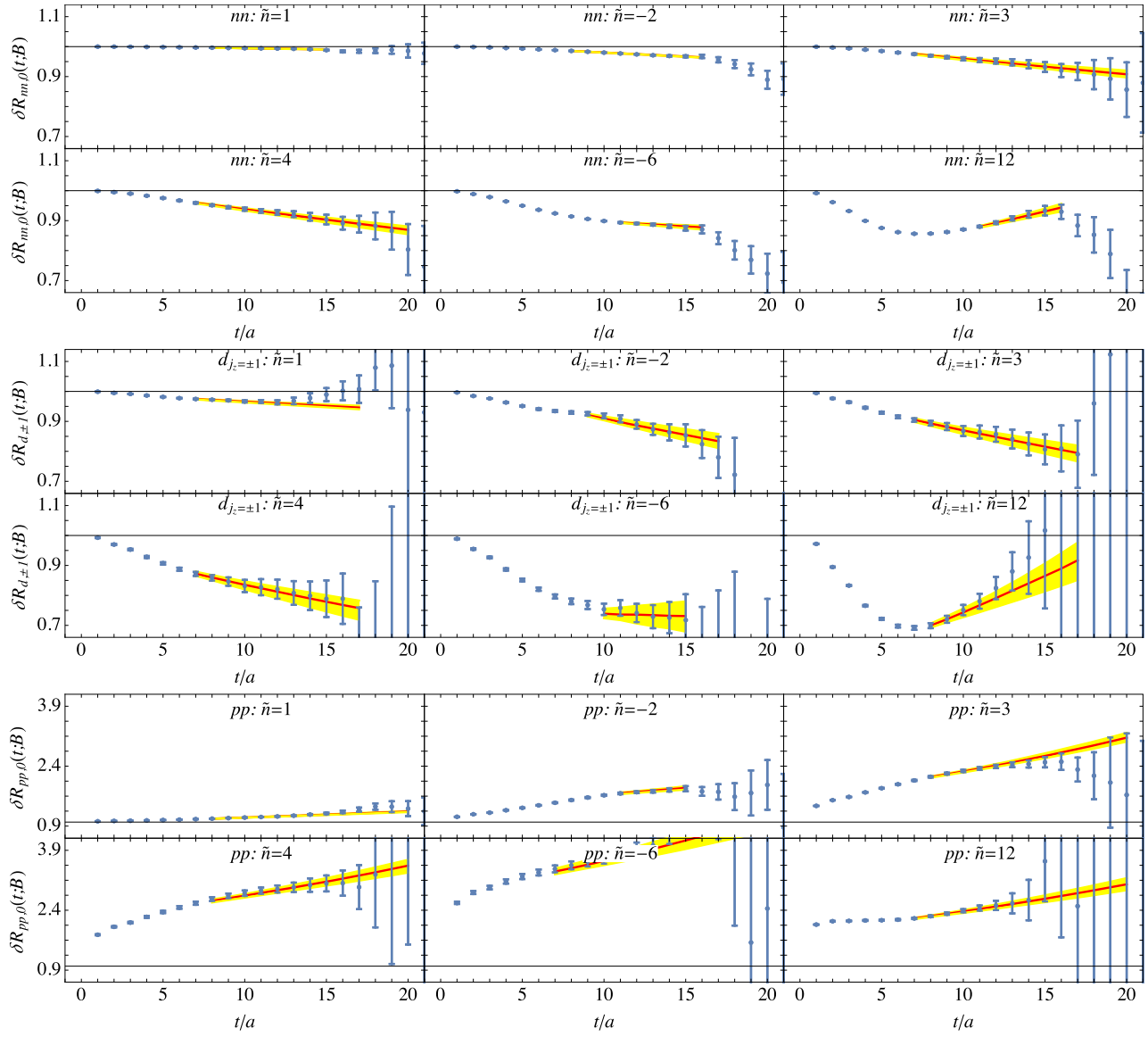

FIG. 4 (color online). The ratios of correlation functions defined in Eq. (14) for the nn, $d(j_z = \pm 1)$, and pp systems. Results are shown for all six magnetic fields for the smeared-smeared correlation functions. The shaded bands correspond to the statistical uncertainties of the given fit. The deuteron spin states are averaged for simplicity.

The pionless EFT [EFT($\not\pi$)] can be used to describe the low-energy strong and electroweak interactions of two-nucleon, three-nucleon, and multinucleon systems [62,63]. It provides a systematic way to include the gauge-invariant electroweak interactions that are not related to strong-interaction S-matrix elements through local multinucleon operators. While conventionally formulated in terms of four-nucleon interactions with insertions of derivatives (as well as higher body interactions), EFT($\not\pi$) can be fruitfully defined in terms of dibaryon fields, permitting a dramatic simplification in calculations beyond leading order (LO) in the expansion [64]. The Lagrange density describing the two-nucleon electromagnetic interactions at LO and next-to-leading order (NLO) in EFT($\not\pi$) using dibaryon fields is [64]

$$\mathcal{L} = \frac{e}{2M_N} N^\dagger [\kappa_0 + \kappa_1 \tau^3] \Sigma \cdot \mathbf{B} N - \frac{e}{M_N} \left(\kappa_0 - \frac{\tilde{l}_2}{r_3} \right) i \epsilon_{ijk} t_i^\dagger t_j B_k + \frac{e}{M_N} \frac{l_1}{\sqrt{r_1 r_3}} [t_j^\dagger s_3 B_j + \text{H.c.}], \quad (15)$$

where t_i are the SO(3) vector components of the ${}^3S_1$ dibaryon field and s_3 is the $I_z = 0$, ${}^1S_0$ dibaryon field, M_N is the nucleon mass, and Σ is the spin operator. The effective ranges in the ${}^1S_0$ and ${}^3S_1$ channels are denoted as r_1 and r_3, respectively, while κ_0 and κ_1 are the isoscalar and isovector magnetic moments of the nucleon. The NLO interactions, described by dibaryon operators coupled to

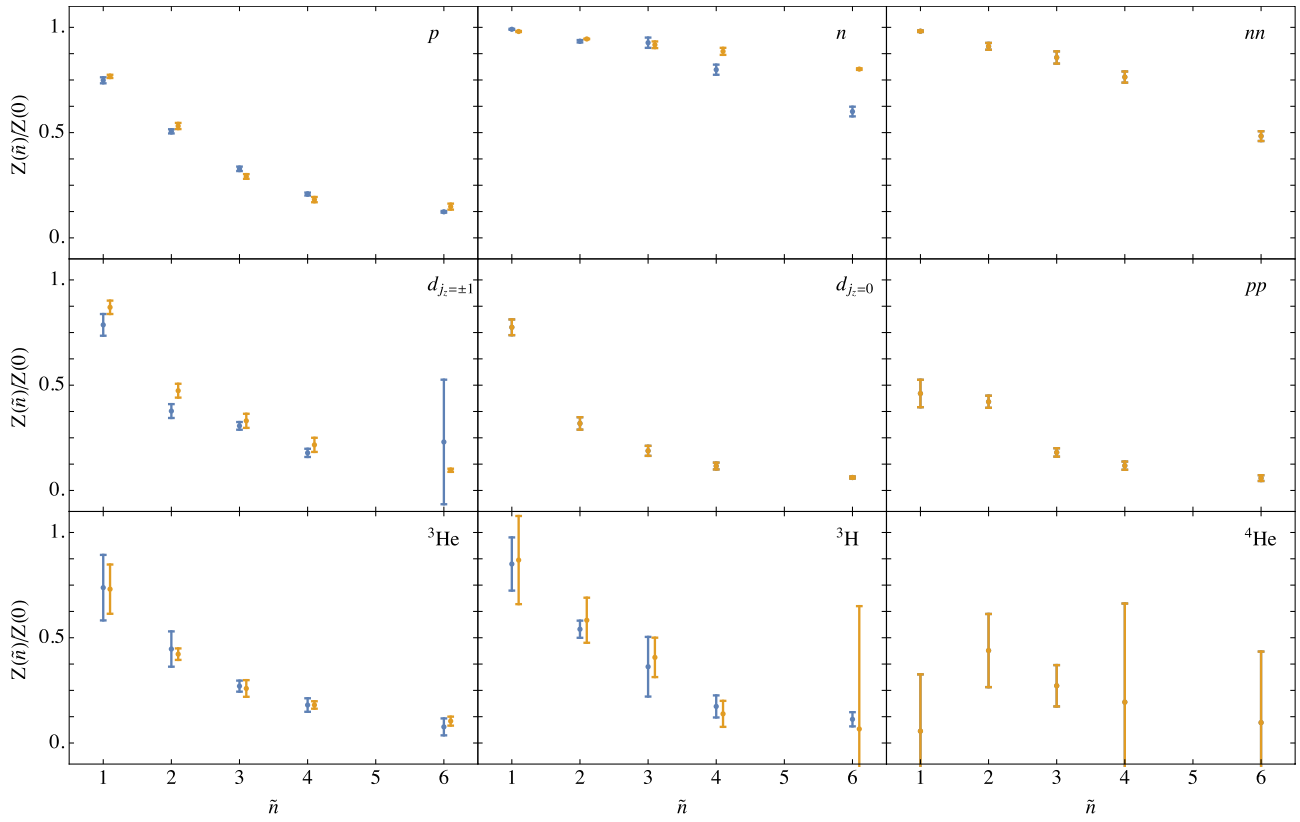

FIG. 5 (color online). The magnetic field strength dependence of the ground state overlap factors, defined in Eq. (10). For $j_z \neq 0$ states, both spin states are shown as the different colored points offset slightly for clarity.

the magnetic field, are accompanied by the coefficients $l_{1,2}$ in Eq. (15).[8]

In Ref. [65], it was recognized that LQCD calculations employing background magnetic fields could be used to extract the deuteron magnetic moment, and the rate for low-energy $np \to d\gamma$ radiative capture, by determining the energy eigenvalues of the two-nucleon systems [65,66]. The deuteron magnetic moment is extracted from the energies of the $j_z = \pm 1$ states in the background fields, while the $np \to d\gamma$ radiative capture cross section is determined from the nucleon isovector magnetic moment and the value of l_1 determined from the energies of the two $j_z = 0$ states in the coupled $^1S_0$-$^3S_1$ np sector. This latter combination is probed through the determinant condition [65]

$$\left[p\cot\delta_1 - \frac{S_+ + S_-}{2\pi L}\right]\left[p\cot\delta_3 - \frac{S_+ + S_-}{2\pi L}\right] = \left[\frac{|e\mathbf{B}|l_1}{2} + \frac{S_+ - S_-}{2\pi L}\right]^2, \tag{16}$$

where $\delta_{1,3}$ are the phase shifts in the $^1S_0$ and $^3S_1$ channels, respectively. Solutions to this equation correspond to the energy eigenvalues of the system, with the functions $S_\pm$ given by

$$S_\pm \equiv S\left(\frac{L^2}{4\pi^2}(p^2 \pm |e\mathbf{B}|\kappa_1)\right), \tag{17}$$

where

$$S(\eta) = \sum_{\mathbf{n}\neq\mathbf{0}}^{|\mathbf{n}|<\Lambda} \frac{1}{|\mathbf{n}|^2 - \eta} - 4\pi\Lambda \tag{18}$$

is the three-dimensional Riemann-zeta function associated with the A_1^+ irreducible representation of the cubic group [67–69].

At the quark masses used in these calculations, the deuteron and bound dineutron are approximately degenerate [34], and have scattering lengths, $a_{1,3}$, and effective ranges, $r_{1,3}$, that are numerically close to each other ($a_1 \sim a_3 = a$ and $r_1 \sim r_3 = r$) [35], and hence $\delta_1 \sim \delta_3 = \delta$.[9] Because of this, Eq. (16) simplifies to

[8] In this expression, l_2 has been replaced by $\tilde{l}_2 - r_3\kappa_0$ to make explicit the deviation of the deuteron magnetic moment, $\mu_d = \frac{e}{M}(\kappa_0 + \frac{\gamma_0}{1-\gamma_0 r_3}\tilde{l}_2)$, from the single nucleon contribution.

[9] The difference in binding energies is $\Delta_{^3S_1,^1S_0} = E_{^1S_0} - E_{^3S_1} = 5.8(1.4)$ MeV [34]; provided the difference in energies is small compared to the shifts induced by the magnetic field, it can be neglected. If it cannot be neglected, the determinant condition must be solved numerically.

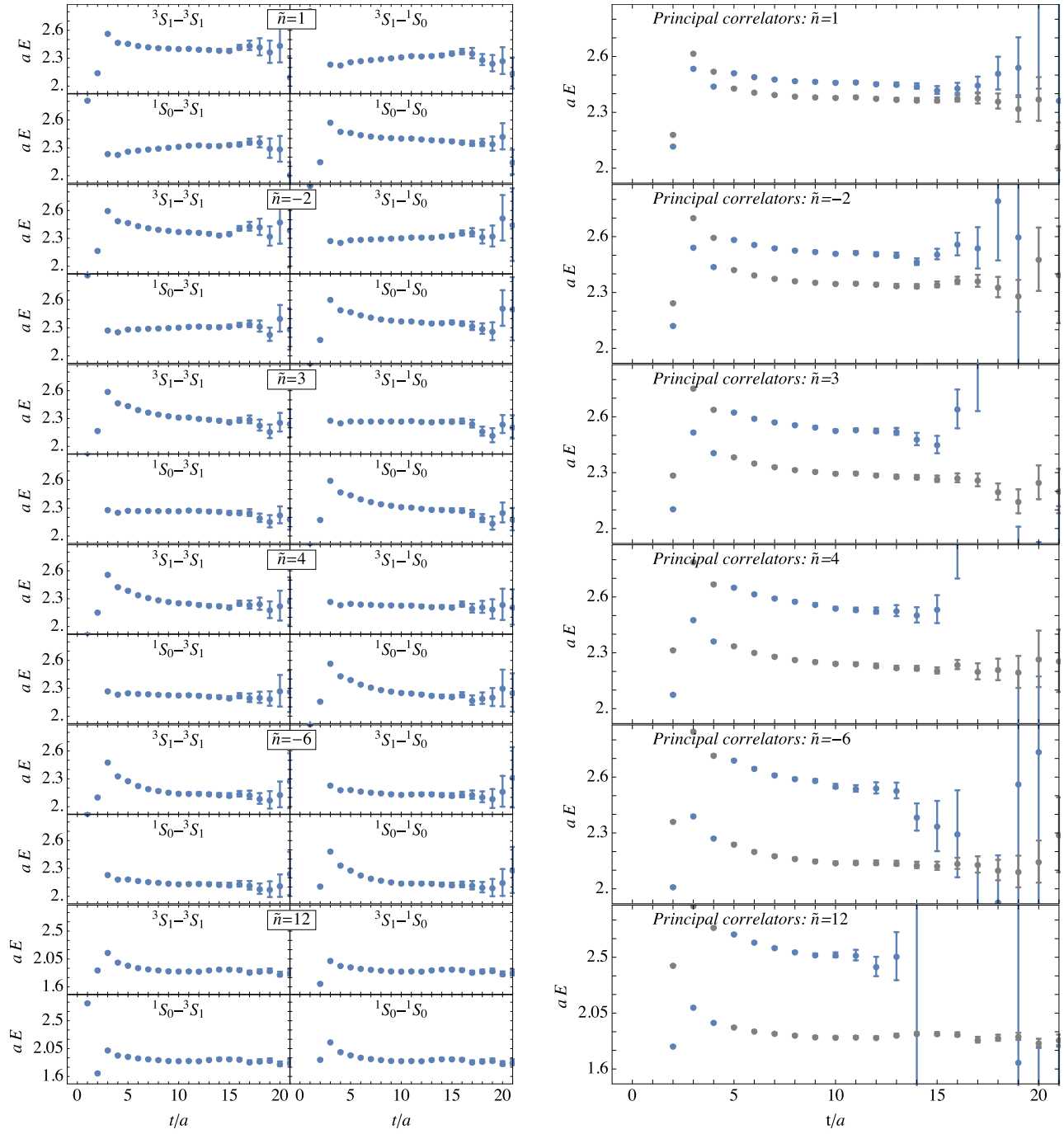

FIG. 6 (color online). Results from nucleon-nucleon smeared-smeared correlation functions in the mixed $j_z = I_z = 0$ sector. The left panels show the effective masses of the elements of the 2×2 matrix of correlation functions, with each quartet of plots corresponding to a different magnetic field strength. In the right panels, the EMPs of the principal correlation functions resulting from solving the associated generalized eigenvalue problem are shown.

$$p \cot \delta = \frac{1}{\pi L} S_{\pm} \pm \frac{|e\mathbf{B}| l_1}{2}, \tag{19}$$

where both signs should be taken together for the two solutions. Expanding this for small $|e\mathbf{B}|$, the shifts in the energies of the two eigenstates are

$$\begin{aligned} \Delta E_{^3S_1,{}^1S_0} &= \mp Z_d^2 (\kappa_1 + \gamma_0 l_1) \frac{|e\mathbf{B}|}{M} + \cdots \\ &= \mp (\kappa_1 + \bar{L}_1) \frac{|e\mathbf{B}|}{M} + \cdots, \end{aligned} \tag{20}$$

where $Z_d = 1/\sqrt{1 - \gamma_0 r}$ is the square root of the residue of the deuteron propagator at the pole and the ellipses

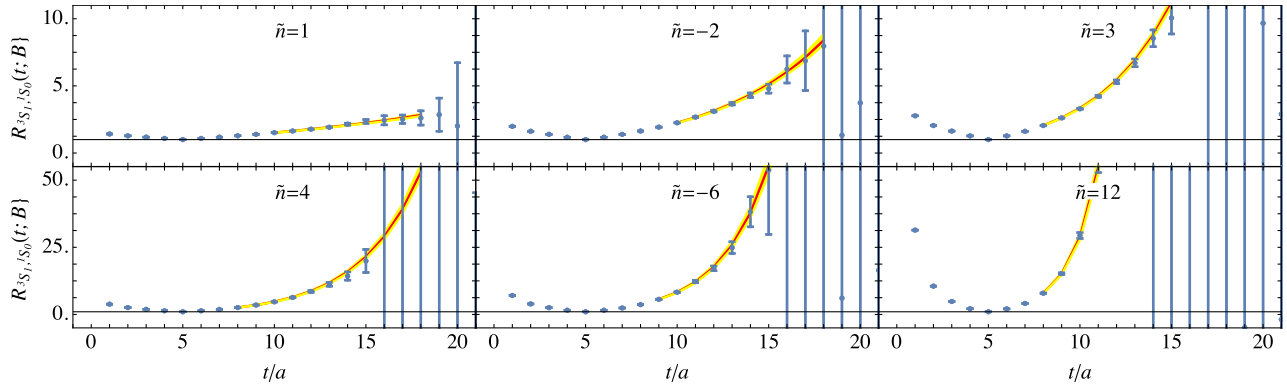

FIG. 7 (color online). The ratio of correlation functions, $R_{^3S_1,^1S_0}(t;\mathbf{B})$, determined from the principal correlation functions for $t_0 = 5$ for all six magnetic field strengths used in this work. Fits to the correlation functions are also shown with uncertainties represented by the shaded region.

denote terms that are higher order in the strength of the magnetic field. In Eq. (20), the deviations of the energy shifts from their naive single-particle values are defined using

$$\bar{L}_1 = \gamma_0 Z_d^2 (l_1 + r\kappa_1). \tag{21}$$

To numerically study this coupled system, it proves useful to first construct the correlation matrix

$$\mathbf{C}(t;\mathbf{B}) = \begin{pmatrix} C_{^3S_1,^3S_1}(t;\mathbf{B}) & C_{^3S_1,^1S_0}(t;\mathbf{B}) \\ C_{^1S_0,^3S_1}(t;\mathbf{B}) & C_{^1S_0,^1S_0}(t;\mathbf{B}) \end{pmatrix}, \tag{22}$$

where the matrix elements $C_{A,B}(t;\mathbf{B})$ are generated from source and sink operators associated with the $A, B \in \{^1S_0, ^3S_1\}$ channels (which are orthogonal in the absence of the magnetic field). The generalized eigenvalue problem, defined by this correlation matrix, can be solved to extract the (diagonalized) principal correlation functions [70], energies, and energy differences. That is, solutions of the system

$$[\mathbf{C}(t_0;\mathbf{B})]^{-1/2}\mathbf{C}(t;\mathbf{B})[\mathbf{C}(t_0;\mathbf{B})]^{-1/2} v = \lambda(t;\mathbf{B}) v \tag{23}$$

are sought, where the eigenvalues are the principal correlation functions $\lambda_\pm(t;\mathbf{B}) = \exp[-(\bar{E} \pm \Delta E_{^3S_1,^1S_0})t]$ with average energy $\bar{E}$ and energy difference $\Delta E_{^3S_1,^1S_0}$. The parameter t_0 can be chosen to stabilize the extraction but has little numerical effect in the current results. To extract the response to a background magnetic field, the ratio of the principle correlation functions,

$$R_{^3S_1,^1S_0}(t;\mathbf{B}) = \frac{\lambda_+(t;\mathbf{B})}{\lambda_-(t;\mathbf{B})} \overset{t\to\infty}{\longrightarrow} \hat{Z} \exp\left[2\Delta E_{^3S_1,^1S_0} t\right], \tag{24}$$

permits a refined determination of the energy difference $\Delta E_{^3S_1,^1S_0}$, significantly reducing correlated fluctuations, where $\hat{Z}$ is a t-independent constant.

Figure 6 shows the EMPs of the original correlation functions of the coupled-channel system in Eq. (22) according to their source and sink types. This figure also shows the EMPs constructed from the principal correlation functions that are determined by solving the generalized eigenvalue problem, Eq. (23), for $t_0 = 5$. The diagonalization of the matrix of correlation functions in Eq. (22) is particularly effective in this case because the states are

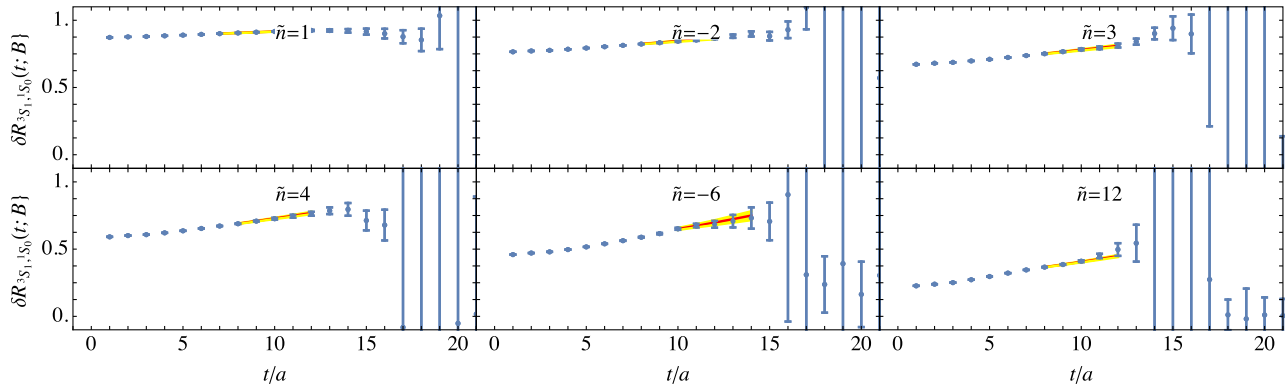

FIG. 8 (color online). The ratio $\delta R_{^3S_1,^1S_0}(t;\mathbf{B})$ computed from the principal correlation functions with $t_0 = 5$, divided by the appropriate isovector combination of the spin differences of the single nucleon correlation functions are shown for all six magnetic field strengths used in this work. Fits to these ratios, and the associated uncertainties (the bands), are also shown.

orthogonal in the limit of vanishing magnetic field. In most cases, plateau behavior is visible in both principal correlation functions, indicating that the lowest two eigenvalues of the system can be extracted. Given this, focus is placed on the ratios $R_{^3S_1,{}^1S_0}(t;\mathbf{B})$ in the region where the principal correlation functions are consistent with single exponential behavior. Figure 7 shows the ratios for all magnetic field strengths along with the associated single exponential fits. Analysis of these ratios in the coupled system is performed with the same methods used to analyze the ratios in the unmixed channels.

As in Eq. (14), the calculated correlation functions associated with nucleons and nuclei share the same quantum fluctuations, to a large degree. This makes it possible to determine differences between properties of the np system and those of a free neutron and proton with more precision than the individual properties. In the current context, the ratio

$$\delta R_{^3S_1,{}^1S_0}(t;\mathbf{B}) = \frac{R_{^3S_1,{}^1S_0}(t;\mathbf{B})}{\Delta R_p(t;\mathbf{B})/\Delta R_n(t;\mathbf{B})} \tag{25}$$

decays with a characteristic exponent $2\Delta E_{^3S_1,{}^1S_0}(\mathbf{B}) - (E_{p,\uparrow} - E_{p,\downarrow}) + (E_{n,\uparrow} - E_{n,\downarrow}) = 2|e\mathbf{B}|\bar{L}_1/M + \mathcal{O}(|\mathbf{B}|^3)$, permitting direct access to deviations from single nucleon physics, where the $\Delta R_h(t;\mathbf{B})$ are given in Eq. (12). Figure 8 shows these ratios for each field strength, from which the energy shifts can be extracted with remarkable precision.

C. Magnetic field strength dependence: General strategies

Having extracted the energies and energy differences as a function of the magnetic field strength, the remaining task is to use them to determine the magnetic properties of the nucleons and nuclei through fits to the expected forms shown in Eq. (7). The fits and extracted properties of each nucleon and nucleus are presented individually in the following subsection. Here, the general features of the analysis, and the difficulties encountered in confronting Landau levels, are discussed.

In dimensionless units, the form used for the fits to the ground states ($\mathbf{B} = B\mathbf{e_z}$ and $P_\parallel = 0$) is

$$\begin{aligned} a\delta E_{h;j_z} = & \sqrt{a^2M_h^2 + (2n_L+1)Q_h a^2|e\mathbf{B}|} \\ & - aM_h - \frac{2e}{aM_N}\hat{\mu}_h j_z a^2|e\mathbf{B}| \\ & - \frac{2\pi}{a^3M_N^2(M_\Delta - M_N)} \\ & \times \left[\hat{\beta}_h + \hat{\beta}_h^{(2)}\left(j_z^2 - \frac{1}{3}j(j+1)\right)\right](a^2|e\mathbf{B}|)^2 \\ & + j_z\hat{\gamma}_h(a^2|e\mathbf{B}|)^3 + \hat{\delta}_h(a^2|e\mathbf{B}|)^4, \end{aligned} \tag{26}$$

where the fit parameters are

$$\begin{aligned} n_L, \quad \hat{\mu}_h &= \mu_h\frac{M_N}{2e}, \ \hat{\gamma}_h, \ \hat{\delta}_h, \\ \hat{\beta}_h &= \frac{M_N^2(M_\Delta - M_N)}{e^2}\beta_h^{(M0)}, \\ \hat{\beta}_h^{(2)} &= \frac{M_N^2(M_\Delta - M_N)}{e^2}\beta_h^{(M2)}, \end{aligned} \tag{27}$$

and $a^2|e\mathbf{B}| = \frac{6\pi|\tilde{n}|}{L^2}$ is the dimensionless field strength. This extends to higher orders in $|e\mathbf{B}|$ than the form given in Eq. (7), providing for estimates of fitting systematic uncertainties in the extraction of the magnetic moments and polarizabilities resulting from the choice of fit form. The hadron masses, aM_h, are taken from our previous studies on this ensemble of gauge-field configurations [34] and are known precisely [$aM_\Delta = 1.3321(10)(19)$ on this ensemble]. For uncharged states, n_L does not enter the fit, and for states with $j = 0$, the parameters $\hat{\mu}$, $\hat{\beta}_h^{(2)}$, and $\hat{\gamma}$ are absent. As in Ref. [29], the extracted magnetic moments are expressed in terms of "natural nuclear magnetons" (nNM) defined with respect to the nucleon mass at the quark masses used in the calculation. The polarizabilities are given in terms of the natural dimensionless polarizability $e^2/M_N^2(M_\Delta - M_N)$ (given the expected dominance of the Δ-resonance, this is the appropriate scale for the magnetic polarizabilities), but are also presented in physical units in the conclusion. A physical interpretation of the higher order parameters is not provided, and they are used only to control the systematic uncertainties in the magnetic moments and polarizabilities extracted from the fit.

In performing fits, the same bootstrap sets of extractions of the energy shifts are used at each magnetic field strength in order to exploit the correlations between them. The ensemble averages of the energy shifts are used to obtain the central values of fit parameters describing the magnetic field strength dependence. An ensemble of fits to the bootstrap data set is used to obtain the associated statistical uncertainties. To propagate the systematic uncertainties from the fits to the ratios of correlation functions into the field dependence analysis, the bootstrap sets of energy shifts are spread away from their mean by the ratio of the quadrature-combined statistical and systematic uncertainties to the statistical uncertainty. That is, for an energy variable E with an ensemble of extracted bootstrap values $\{E_i\}$, mean value $\bar{E} = \frac{1}{N_B}\sum_{b=1}^{N_B} E_b$, and statistical and fitting systematic uncertainties δE_{stat} and δE_{sys}, the spread bootstrap ensemble values $\{\tilde{E}_i\}$ are taken to be

$$\tilde{E}_i = \bar{E} + \frac{\sqrt{\delta E_{\text{stat}}^2 + \delta E_{\text{sys}}^2}}{\delta E_{\text{stat}}}(E_i - \bar{E}), \tag{28}$$

and it is these quantities that are used in subsequent analyses. The highly correlated nature of the results

obtained at different field strengths (that is, results obtained at different magnetic field strengths on a given configuration have correlated statistical fluctuations) makes this approach essential.

An important aspect of the present analysis is to address the range of magnetic field strengths for which the fit forms in Eq. (26) describe the energy shifts. This is addressed by varying the number of magnetic field strengths used in the fits, fitting results obtained at $|\tilde{n}| \leq \tilde{n}_{\max}$ with $\tilde{n}_{\max} = 2, 3, 4, 6, 12$. The complexity of the fit form is also varied either by using the full form or by setting $\hat{\delta} = 0$, $\hat{\delta} = \hat{\gamma} = 0$, or $\hat{\delta} = \hat{\gamma} = \hat{\beta} = 0$. Further, either the smeared-sink or point-sink correlation functions are selected for fitting. For $j = 0$ states, a total of $4 \times 2 \times 2 = 16$ different fits are considered for each bootstrap ensemble. For the $j > 0$ states, coupled fits were performed to the magnetic field strength dependence of the $j_z = \pm j$ spin states, and $5 \times 4 \times 2 = 40$ different fits are considered for each bootstrap ensemble. A large number of fits successfully described the results with an acceptable χ^2/d.o.f., although some did not. The central values and uncertainties in the extracted parameters are evaluated from the distribution of the results for the acceptable fits and are taken as the 50th quantile and the 17th–83rd range of quantiles, respectively. As an additional check, we have used the Bayes information criterion for a given fit to assess those that are acceptable and find uncertainties that are consistent with those defined from the χ^2.

A further complication arises from the Landau-level nature of the eigenstates and the suboptimal projection of the interpolating operators onto them. In every case, correlation functions that have single exponential behavior over a significant range of time slices are found. However, it is clear that these states do not correspond to the lowest Landau level. Expanding the field dependence in the nonrelativistic limit, the magnetic moment contribution cancels in the spin-averaged energy shift, but a linear contribution survives with a coefficient determined by n_L,

$$a[E_{h;j_z}(\mathbf{B}) + E_{h;-j_z}(\mathbf{B})] = \frac{a^2 Q_h |e\mathbf{B}|}{2aM_h}(2n_L + 1) + \mathcal{O}(|\mathbf{B}|^2), \tag{29}$$

where the masses are precisely known from previous studies [34]. From examining the small field shifts for charged states, it is found that $n_L \neq 0$ in all cases. Thus, the interpolating operators overlap strongly onto excited states of the system and presumably will relax to the ground state only at large Euclidean times. Because of this, n_L is treated as a fit parameter and the fits themselves are used to determine which Landau levels are dominating the various correlation functions. In the limit of vanishing lattice spacing, and neglecting structure effects, the allowed values of n_L are integers, and a somewhat complicated approach to fitting is required. Two alternate procedures are considered. In the first approach, the lowest magnetic field strengths are used to determine the linear term in the field-strength dependence, which is used to identify the integer value of n_L that is most consistent with the numerical results. This value is held fixed and then used in further fits utilizing the full form of Eq. (26). In the second approach, n_L is first treated as a real-valued fit parameter and the full fits are performed. Then, after considering the different fits, the integer $\hat{n}_L$ closest to the mean of successful fits is chosen and held fixed in the final set of fits.[10] An additional systematic is assessed by combining sets of fits (varying fit forms, data ranges, and types of correlation functions) with $\hat{n}_L \to \hat{n}_L \pm 1$ into the full suite of fits (for charged, $j > 0$ states, a total of 120 different fits are considered for each bootstrap ensemble). Both choices of Landau-level procedures lead to consistent results after these systematic uncertainties are taken into account.

A related systematic uncertainty that is considered is the potential ambiguity in identifying the Landau level associated with the plateau at each magnetic field strength. In the fitting forms, it is implicit that the energies of a nucleon or nucleus result from a single Landau level for the range of magnetic fields that are considered. This is expected to be the case at small magnetic fields, but might not be valid at larger magnetic fields. To explore this issue, fit forms with different $\hat{n}_L$ for different magnetic fields are considered. Keeping only the results from the lowest four magnetic fields, and allowing different values of $\hat{n}_L$ for each magnetic field does not result in acceptable fits except when the $\hat{n}_L$'s are all the same. This leads to confidence in the assumption that the same Landau state is providing the energies that are dominating the fits.

D. The magnetic properties of nucleons and nuclei

1. The neutron

The neutron correlation functions and their ratios for each spin component and magnetic field strength used in this analysis, along with the associated fits, are shown in Figs. 1 and 2, and the energy shifts extracted from these functions are presented in Table I. Figure 9 shows the energy shifts of a spin-up and a spin-down neutron as a function of the background magnetic field strength. The two spin states behave quite differently in the presence of the magnetic field. The energy shift of the spin-down state (negatively shifted as the neutron magnetic moment is negative) responds almost linearly to the magnetic field, even out to $|e\mathbf{B}| \sim 0.71$ GeV^2 ($\tilde{n} = 12$), while the response of the spin-up state exhibits significant nonlinearities even

[10]The extractions of magnetic moments and the $np \to d\gamma$ cross section are independent of these complications as the Landau-level contributions cancel in the energy differences between spin states.

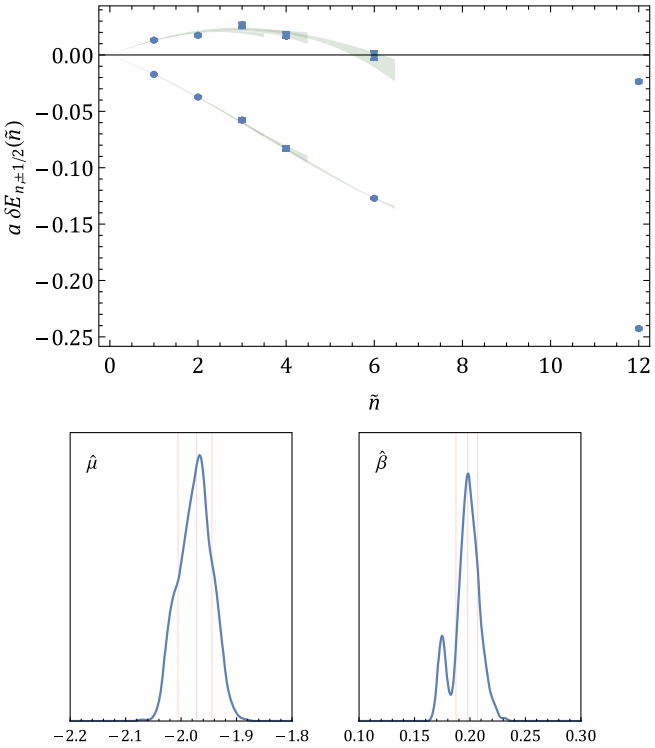

FIG. 9 (color online). Results for the energy shifts of a spin-up (upper points) and a spin-down (lower points) neutron in a background magnetic field. The central 68th quantile of successful fits is shown as the shaded bands. Different overlapping bands are shown for fits over the different ranges of $\tilde{n}$. The lower panel shows the probability-density functions for the relevant fit parameters $\hat{\mu}$ and $\hat{\beta}$, with the vertical lines indicating the central value and uncertainties.

for modest magnetic fields. The behavior of the spin-up state is reminiscent of the lower level in a two-state system with an avoided level crossing. Given the expected tower of QCD excitations of the nucleon, the observed behavior of the spin-up state is consistent with the magnetic field inducing mixing between the spin-up neutron and higher-lying states. Such mixing is expected from quark-hadron duality, and LQCD calculations that also probe the response of excited states to the magnetic field could be used to investigate this further. This behavior implies that spin-dependent polarizabilities are highly correlated with spin-independent polarizabilities, and it will be interesting to learn if this pattern persists as the quark masses are brought closer to their physical values.

As discussed in the previous subsection, a large number of different fits involving varying ranges of field strengths and with a variety of functional forms are performed in order to analyze the energy shifts and determine the magnetic moment and polarizability. The 17th and 83rd quantile range of all successful fits to each data range are shown as the shaded regions in Fig. 9. Separate (overlapping) regions are shown for each data range $\tilde{n} \leq n_{\max}$ for which successful fits were found. Note that the figure shows the results from smeared-smeared correlation functions only, but the fits that are considered also include those involving the energies extracted from smeared-point correlators. The figure also shows the probability density functions (PDFs) generated from combining the central values of all successful fits (considering fits over the energy shifts extracted from each of the bootstrap ensembles) for the two relevant parameters, $\hat{\mu}$ and $\hat{\beta}$. For fits involving additional parameters, these are integrated over, while for linear fits just involving the magnetic moment, these are ignored in determination of the PDF for $\hat{\beta}$. Analysis of the suite of fits that are detailed in the previous subsection yields a neutron magnetic moment and polarizability of

$$\hat{\mu}_n = -1.972\begin{pmatrix}+0.027\\-0.033\end{pmatrix}(0.059), \tag{30}$$

$$\hat{\beta}_n = 0.198\begin{pmatrix}+0.009\\-0.011\end{pmatrix}(0.010), \tag{31}$$

where the first uncertainties combine the statistical and systematic uncertainties from the extraction of the energy shifts, as well as the systematic uncertainty from the fit to the magnetic field strength. The second uncertainty estimates the effects of discretization and finite volume effects; as discussed in the conclusion this is assessed to be a 3% multiplicative uncertainty on magnetic moments and a 5% multiplicative uncertainty on polarizabilities. The above results are presented in the natural dimensionless units, and the values of the magnetic moment and polarizability in physical units are subject to additional uncertainties from the lattice scale-setting procedure, which are discussed in the conclusion. The magnetic polarizability and magnetic moment of the neutron have been calculated previously with LQCD over a range of light-quark masses [39,43] albeit with large uncertainties. The calculated magnetic moment is consistent with previous calculations at similar quark masses, and the value of β_n is also consistent with previous calculations [43].[11]

2. The dineutron

At these unphysical quark masses, the dineutron (in the $^1S_0$ channel) is a bound state, with a binding energy of $B_{nn} = 16(5)$ MeV [34]. As it is electrically neutral, composed of two neutrons in the $^1S_0$ channel with positive parity, the dineutron provides the simplest nuclear system with which to explore the effects of binding on magnetic properties. This system is discussed before proceeding to states that are electrically charged and therefore complicated by the presence of Landau levels.

[11]The authors of Ref. [43] report difficulties in identifying ground states.

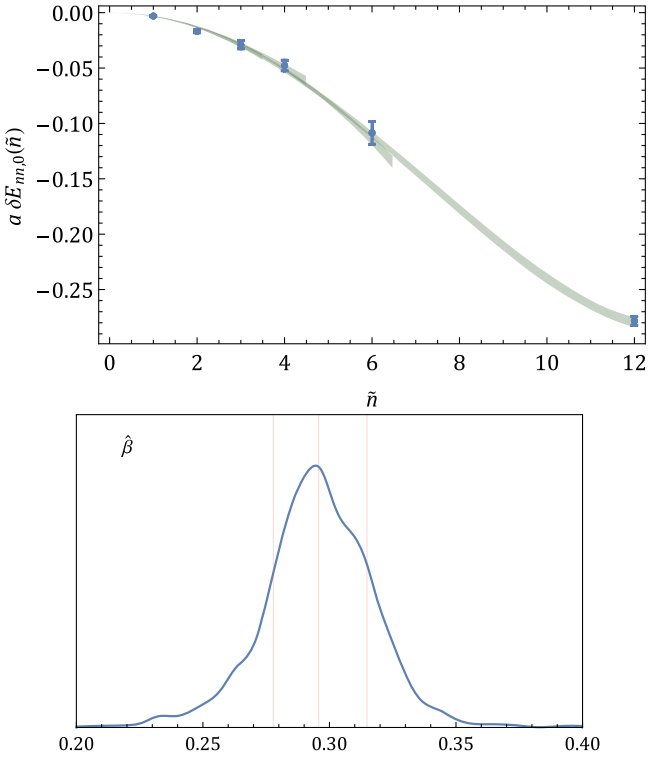

FIG. 10 (color online). The energy shifts of the dineutron as a function of the background magnetic field strength, $\tilde{n}$. The details of the figure are as in Fig. 9. The lower panel shows the PDF for the dineutron polarizability.

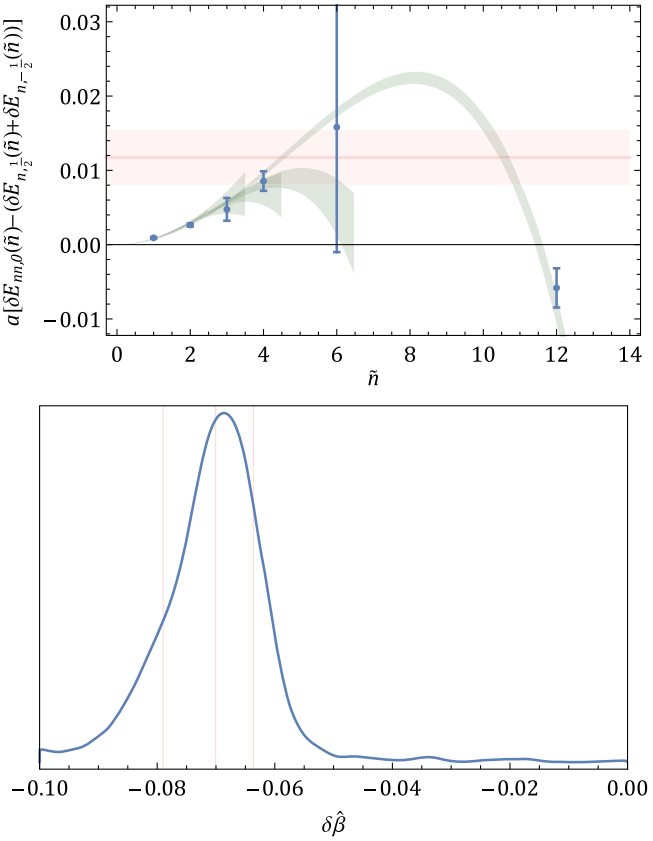

FIG. 11 (color online). Results for the difference between the energy shifts of the dineutron and a spin-up and a spin-down neutron as a function of the background magnetic field strength. The green shaded regions are the result of the suite of fits to the field strength dependence. The horizontal red-shaded region shows the breakup threshold for the dineutron, above which the ground state of the system would be two neutrons in the continuum in the ${}^1S_0$ channel.

Figures 1 and 2 show the dineutron correlation functions and the ratios of correlation functions for each field strength, along with fits to the time dependence of the ratios. The energy shifts extracted from the ratios of correlation functions are given in Table I for each field strength, and Figure 10 shows these shifts. Combining all of the attempted fits to the energy shifts, as described in detail for the neutron, yields a magnetic polarizability of

$$\hat{\beta}_{nn} = 0.296\begin{pmatrix}+0.019\\-0.018\end{pmatrix}(0.015), \tag{32}$$

where the uncertainties are as for the case of the neutron, and the result is presented in the dimensionless natural units of the system, defined in Eqs. (26) and (27).

This polarizability is significantly smaller than twice the single neutron polarizability with $\delta\hat{\beta}_{nn} \equiv \hat{\beta}_{nn} - 2\hat{\beta}_n \sim 0.1$. This difference can also be obtained from the ratio $\delta R_{nn,0}(t;\mathbf{B})$ in Eq. (14) that probes the difference directly in a correlated manner. In the large time limit, the exponential decay of this ratio is governed by the energy difference $\delta E_{nn}(\mathbf{B}) - \delta E_{n,\frac{1}{2}}(\mathbf{B}) - \delta E_{n,-\frac{1}{2}}(\mathbf{B})$. These ratios are displayed in Fig. 4 for the different field strengths, and the extracted energy shifts are shown in Fig. 11 as a function of the field strength. In turn, $\delta\hat{\beta}_{nn}$ is the coefficient of the quadratic term in the field strength dependence of this energy difference. Analyzing these energy shifts using the same methods as above leads to

$$\delta\hat{\beta}_{nn} \equiv \hat{\beta}_{nn} - 2\hat{\beta}_n = -0.070\begin{pmatrix}+0.006\\-0.009\end{pmatrix}(0.004). \tag{33}$$

As discussed above, the neutron spin-down state is magnetically rigid and remains undeformed even at large magnetic fields, while the spin-up state is strongly deformed. For the dineutron, the overall energy is lowered in a magnetic field, driven largely by the spin-down neutron. As this also lowers the energy of the spin-up neutron, it has a reduced mixing with other states and, therefore, becomes more rigid. From Fig. 11, it is apparent that the binding energy of the dineutron (the energy required to separate the spin-up and spin-down neutron) is reduced for $\tilde{n} \lesssim 8$, but is larger for $\tilde{n} = 12$ than at $\mathbf{B} = 0$. If this behavior persists at the physical quark masses, it would indicate that it is energetically disfavored for neutron matter (or near-neutron matter) in dense stellar objects to spontaneously generate a magnetic field through the

formation of dineutron pairs. It is also interesting to note that at intermediate field strengths, the dineutron system is nearing a Feshbach resonance in which the binding energy is approaching zero and the scattering length is approaching infinity.

3. The proton

The analysis of the proton in a magnetic field is more complicated than that of the neutron and dineutron. As discussed previously, the interpolating operators used in this work project onto plane waves in all three spatial directions rather than Landau levels which we expect to be closer to the eigenstates of the system, so the quality of the correlation functions for charged systems is expected to be significantly worse than that for electrically neutral systems. This is indeed the case, as can be seen from the EMPs shown in the first row of Fig. 1; in comparison to the neutron, the proton correlation functions are of lower quality with plateaus setting in at later times and with significantly larger uncertainties. Further, the presence of Landau levels significantly complicates the spectrum of a charged system, and it is clear that the plateaus that are evident do not correspond to the lowest Landau level, as discussed above. The Landau level associated with the plateau is identified through systematic analysis of the field-strength dependence, as discussed in Sec. III C.

In Fig. 2, the ratios of correlation functions associated with each spin component and field strength, and associated fits, are shown. The energy shifts resulting from these fits are given in Table I for each magnetic field strength and are shown in Fig. 12. The suite of fits that are performed lead to a proton magnetic moment and polarizability of

$$\hat{\mu}_p = 3.17\begin{pmatrix}+0.10\\-0.09\end{pmatrix}(0.09), \tag{34}$$

$$\hat{\beta}_p = 0.83\begin{pmatrix}+0.10\\-0.07\end{pmatrix}(0.04), \tag{35}$$

where the uncertainties are as discussed for the case of the neutron, and the results are presented in the dimensionless natural units defined in Eqs. (26) and (27). The Landau level makes a contribution to the $\mathcal{O}(B^2)$ term that is suppressed by the mass of the proton, and its main contribution is to the term linear in B where it can be well constrained by the coupled analysis of the two spin states. Consequently, the uncertainty in identifying the correct Landau level of the system does not lead to a particularly large uncertainty in the extracted value of its magnetic polarizability (although the neutron polarizability is considerably more precise).

The magnetic polarizability of the proton is found to be considerably larger than that of the neutron, $\hat{\beta}_p - \hat{\beta}_n = 0.63(10)(4)$, indicating a significant isovector component

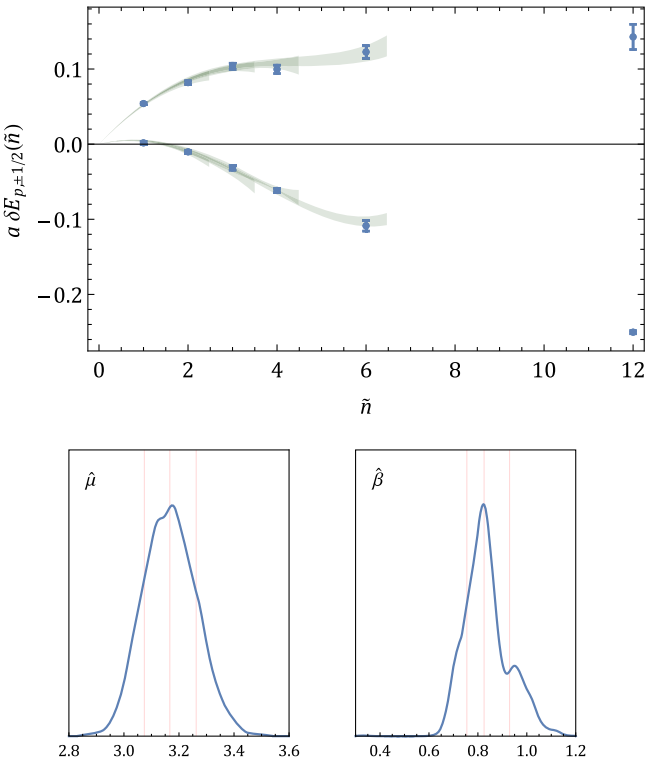

FIG. 12 (color online). Results for the energy shifts of a spin-up (lower points) and a spin-down (upper points) proton in a uniform background magnetic field. The details of the figure are as in Fig. 9. The lower panel shows the PDFs for the fit parameters $\hat{\mu}$ and $\hat{\beta}$.

at this unphysical pion mass. Currently, there are no other LQCD calculations of the proton magnetic polarizability with which to compare; however, it can be compared with the experimental value. As quoted previously, $\beta_p^{\text{phys}} = 3.15(0.35)(0.2)(0.3) \times 10^{-4}$ fm^3 [2–7] which corresponds to $\hat{\beta}_p^{\text{phys}} = 0.116(13)(7)(11)$ in dimensionless units. The physical value results from cancellations between pion-loop (chiral physics) and Δ-pole contributions that are both $\mathcal{O}(10 \times 10^{-4}$ fm$^3)$. Since the pion-loop contribution is strongly suppressed at heavy quark masses and the Δ-pole contribution depends less strongly on mass, the size of the magnetic polarizability determined at the SU(3) point is in line with expectations.

4. The diproton

The diproton is in the same $^1S_0$ isotriplet as the dineutron and, neglecting the electroweak interactions and the difference in mass between the up and down quarks, it would have the same properties as the dineutron at zero magnetic field. However, the presence of the background magnetic field breaks isospin symmetry through the light-quark electric charges, so the diproton magnetic properties are expected to be quite different from the dineutron, even neglecting the issue of Landau levels.

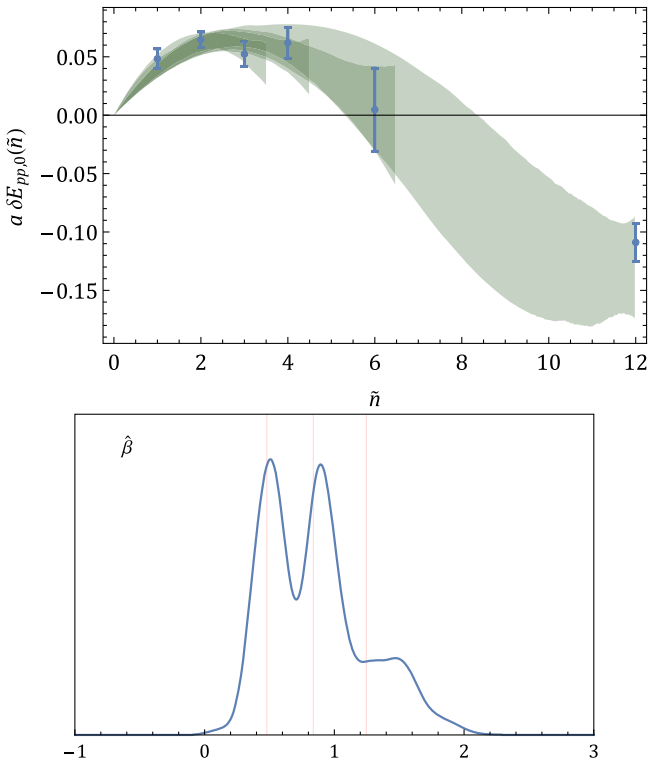

FIG. 13 (color online). Results for the energy shifts of the diproton as a function of the background magnetic field strength. The details are as those in Fig. 10. The lower panel shows the PDFs for the fit parameter $\hat{\beta}$.

Extracting energy differences from fits to the ratios of correlation functions shown in Fig. 2 leads to the results shown in Fig. 13. Fitting the energy shifts, as discussed previously, allows for an extraction of the diproton polarizability of

$$\hat{\beta}_{pp} = 0.84\begin{pmatrix}+0.41\\-0.36\end{pmatrix}(0.04). \tag{36}$$

As in the case of the dineutron, the correlated ratios of the diproton and the spin-up and spin-down proton correlation functions directly determines the difference of energy splittings. Figure 4 shows these ratios, leading to the energy shifts shown in Fig. 14. The figure also shows the envelopes of the ensemble of acceptable fits that were performed using polynomials of up to quartic order.

It is clear from Fig. 14 that the magnetic field strengthens the binding of the diproton by a significant amount that rapidly increases until $\tilde{n} \sim 3$ and then remains constant for larger field strengths. This behavior is interesting in the context of the suggestion that at the physical quark masses, the diproton can overcome the Coulomb repulsion and form a bound state [71] in a strong enough magnetic field, although this argument requires the system to be near unitarity. However, the form of the difference is more complicated in this case than for the dineutron because the

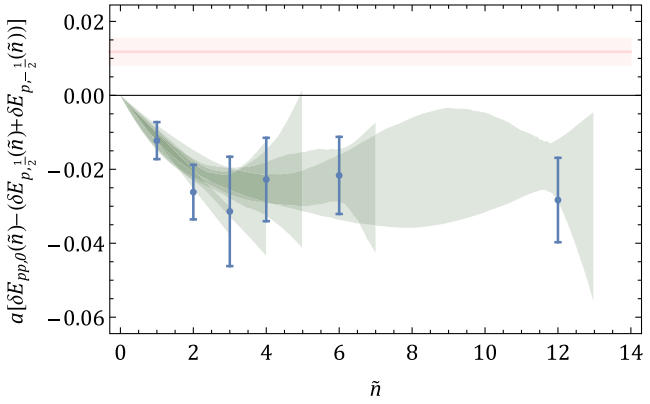

FIG. 14 (color online). Results for the difference between the energy shifts of the diproton and a spin-up and a spin-down proton as a function of the background magnetic field strength. The red-shaded region corresponds to the breakup threshold, above which the ground state of the system would be two protons in the continuum in the $^1S_0$ channel.

contributions of Landau levels in the diproton and spin averaged protons may be different. The difference in magnetic polarizabilities is therefore estimated in the naive way, giving

$$\delta\hat{\beta}_{pp} = -0.82\begin{pmatrix}+0.42\\-0.37\end{pmatrix}(0.04), \tag{37}$$

where the uncertainties of the diproton and proton polarizabilities are combined in quadrature.

5. The deuteron: $j_z = \pm 1$

The deuteron is a bound state in the positive parity $^3S_1$-$^3D_1$ coupled channels. In a background magnetic field, while the $j_z = \pm 1$ states remain isolated in the $^3S_1$-$^3D_1$ coupled channels (in infinite volume), the $j_z = 0$ state mixes with the positive parity $^1S_0$ isotriplet np channel. Here, the focus is on the $j_z = \pm 1$ states which are used to extract the magnetic moment and a combination of the scalar and tensor polarizabilities. The $j_z = I_z = 0$ coupled states are addressed in the following subsection.

Figure 1 shows the effective masses resulting from the $j_z = \pm 1$ deuteron correlation functions, and Fig. 3 shows the ratios of these correlation functions, along with fits to their time dependence. The energy shifts extracted from these ratios are shown in Fig. 15. Analysis of the field strength dependence through a suite of coupled fits to the two spin states, as discussed above, leads to a magnetic moment and polarizability of

$$\hat{\mu}_d = 1.41\begin{pmatrix}+0.28\\-0.25\end{pmatrix}(0.04), \tag{38}$$

$$\hat{\beta}_d^{(M0)} + \frac{1}{3}\hat{\beta}_d^{(M2)} = 0.70\begin{pmatrix}+0.24\\-0.23\end{pmatrix}(0.04). \tag{39}$$

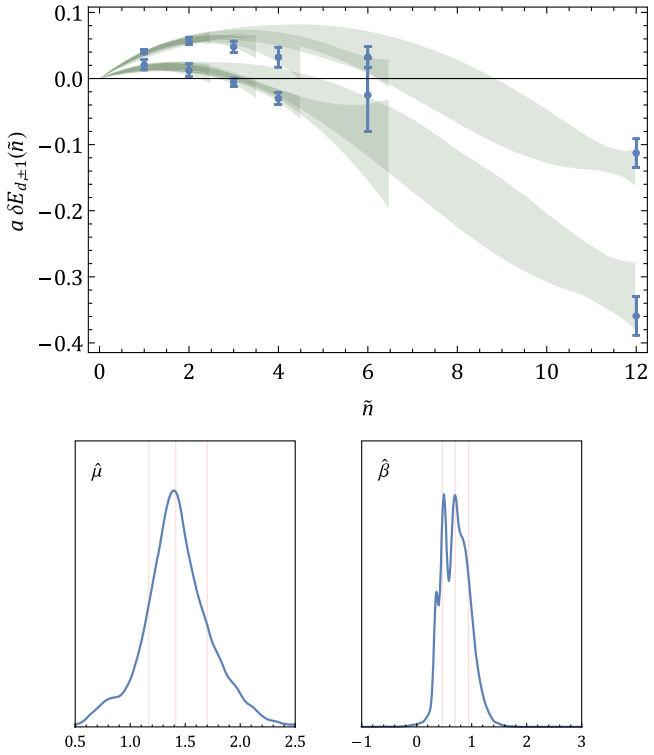

FIG. 15 (color online). Results for the energy shifts of the deuteron in the $j_z = \pm 1$ states as a function of the background magnetic field strength (the lower points correspond to the $j_z = +1$ state). The details of the figure are as in Fig. 10. The lower panel shows the PDFs for the fit parameters $\hat{\mu}$ and $\hat{\beta}$.

As the deuteron has $j = 1$, both the scalar and the tensor polarizabilities contribute to the quadratic dependence on the magnetic field strength, as presented in Eq. (7).[12]

The sum of the proton and neutron magnetic polarizabilities at this pion mass is $\hat{\beta}_p + \hat{\beta}_n \sim 1.02(^{+0.10}_{-0.07})(0.05)$, so the deuteron in the $j_z = \pm 1$ states is somewhat more magnetically rigid than the sum of its constituents. While they cannot be separated from this result alone, the nuclear forces and gauge-invariant electromagnetic two-nucleon operators are responsible for this difference. It will be interesting to learn whether this difference persists at the physical quark masses. Figure 16 shows the splitting between the $j_z = \pm 1$ spin states of the deuteron and the breakup threshold as a function of the field strength. As in the case of the dineutron, the magnetic field pushes the $j_z = \pm 1$ spin states of the deuteron toward threshold, and at $\tilde{n} \sim 5$, the deuteron becomes potentially unbound before rebinding at larger field strengths. The figure also shows the envelopes of the ensemble of acceptable fits that we perform using

[12]With further analysis, the $\mathcal{O}(|e\mathbf{B}|^2)$ shifts in the $j_z = 0$ np coupled system should determine an orthogonal combination of the scalar and tensor polarizabilities, $\hat{\beta}_d^{(M0)} - \frac{2}{3}\hat{\beta}_d^{(M2)}$ as given in Eq. (7), but this extraction is not pursued in the present study.

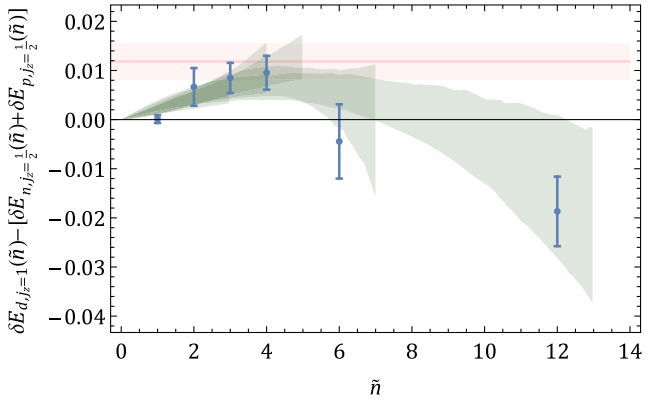

FIG. 16 (color online). Results for the difference between the energy shifts of the $j_z = +1$ spin states of the deuteron and that of a spin-up neutron and spin-up proton as a function of the background magnetic field strength. The red-shaded horizontal band corresponds to the breakup threshold, above which the ground state of the system would be a proton and a neutron in the $^1S_0$ continuum. The green shaded regions correspond to the envelopes of the fits discussed in the main text.

polynomials of up to quartic order. As for the case of the diproton, the presence of Landau levels that may differ between the deuteron and the proton complicates the analysis of the field strength dependence, and we do not report a value of $\delta\beta_d$.

6. ^{3}He

At the physical quark masses, ^{3}He can be thought of, to a large degree, as two protons spin paired in the $^1S_0$ channel and a single unpaired S-wave neutron. The ground state is positive parity with spin half and is an isospin partner with the ground state of the triton, ^{3}H. A naive shell-model prediction is that the magnetic moment of the ground state of ^{3}He is that of the neutron (with the spin-paired protons not contributing) and that the magnetic moment of the ground state of the triton is that of the proton (with the spin-paired neutrons not contributing). The experimental values of both magnetic moments deviate only slightly from these naive predictions. Recent calculations have shown that this feature persists even at heavier quark masses [29], in particular, at the pion mass employed in the present analysis.

The EMPs obtained from the ^{3}He correlation functions in the background magnetic fields are shown in Fig. 1, and the ratios of correlation functions for each spin state are shown in Fig. 3, along with fits to their time dependence. The quality of these ratios is inferior to those obtained in the one-nucleon and two-nucleon sectors, but strong signals are still evident. The energies that are extracted from these ratios are shown in Fig. 17. Analysis of the field strength dependence of the two spin states allows the magnetic responses to be determined, leading to a magnetic moment and polarizability of ^{3}He of

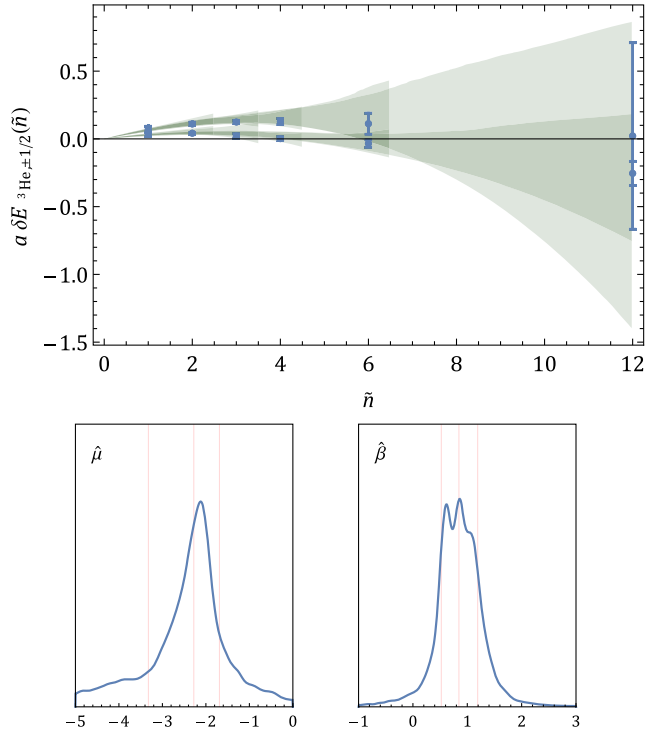

FIG. 17 (color online). Results for the energy shifts of ^{3}He as a function of the background magnetic field strength along with the fit envelopes. The details of the figure are as in Fig. 10. The lower energy points correspond to the $j_z = -\frac{1}{2}$ state, while the upper points correspond to $j_z = +\frac{1}{2}$. The lower panel shows the PDFs for the fit parameters $\hat{\mu}$ and $\hat{\beta}$.

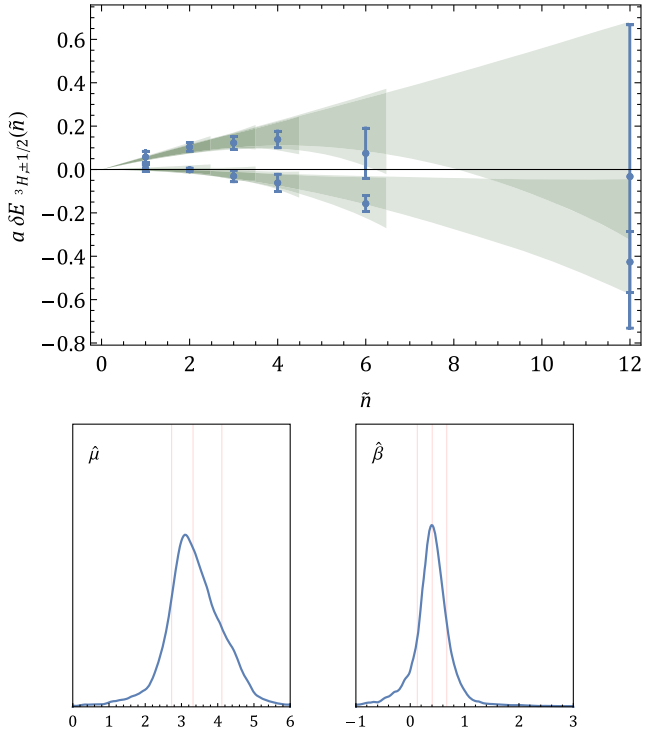

FIG. 18 (color online). Results for the energy shifts of ^{3}H as a function of the background magnetic field strength, along with envelopes of fits. The details of the figure are the same as in Fig. 10. The lower energy points correspond to the $j_z = +\frac{1}{2}$ state, while the upper points correspond to $j_z = -\frac{1}{2}$. The lower panel shows the PDFs for the fit parameters $\hat{\mu}$ and $\hat{\beta}$.

$$\hat{\mu}_{^3\mathrm{He}} = -2.28\begin{pmatrix}+0.59\\-1.04\end{pmatrix}(0.07), \tag{40}$$

$$\hat{\beta}_{^3\mathrm{He}} = 0.85\begin{pmatrix}+0.34\\-0.32\end{pmatrix}(0.04), \tag{41}$$

in natural dimensionless units. Within the uncertainties of the calculations, the polarizability of ^{3}He is consistent with the sum of polarizabilities of its constituent diproton and neutron. This is somewhat surprising given that the magnetic polarizability of such a state would be determined in part by its binding energy and is not expected to be a simple sum over constituent polarizabilities. The uncertainties in the magnetic polarizabilities of ^{3}He are sufficiently large that statistically significant deviations from the contributions from the one-body contribution are not obtained, and hence we have no meaningful constraint on the MEC contributions.

7. The triton

As in the case of ^{3}He, the ratios of the triton correlation functions are significantly less well defined than those in the one-body and two-body sectors. The energy shifts extracted from the correlation functions are shown in Fig. 18. Fits to the magnetic field strength dependence of the energies of the two spin states enable an extraction of the magnetic moment and polarizability of the triton of

$$\hat{\mu}_{^3\mathrm{H}} = 3.32\begin{pmatrix}+0.79\\-0.59\end{pmatrix}(0.10), \tag{42}$$

$$\hat{\beta}_{^3\mathrm{H}} = 0.40\begin{pmatrix}+0.27\\-0.27\end{pmatrix}(0.02). \tag{43}$$

The value of the triton polarizability is considerably smaller than the naive expectation of the sum of the polarizability of the dineutron and of the proton, $\beta_p + \beta_{nn} = 1.12(^{+0.11}_{-0.07})$, and this difference could potentially be used to provide a constraint on two- and three-nucleon electromagnetic interactions.

8. ^{4}He

The ^{4}He nucleus has the quantum numbers of two protons and two neutrons in a spin-zero, even-parity configuration. The energy of the ground state has been determined at unphysical quark masses in previous LQCD calculations [34,72–74], and at this pion mass it is bound

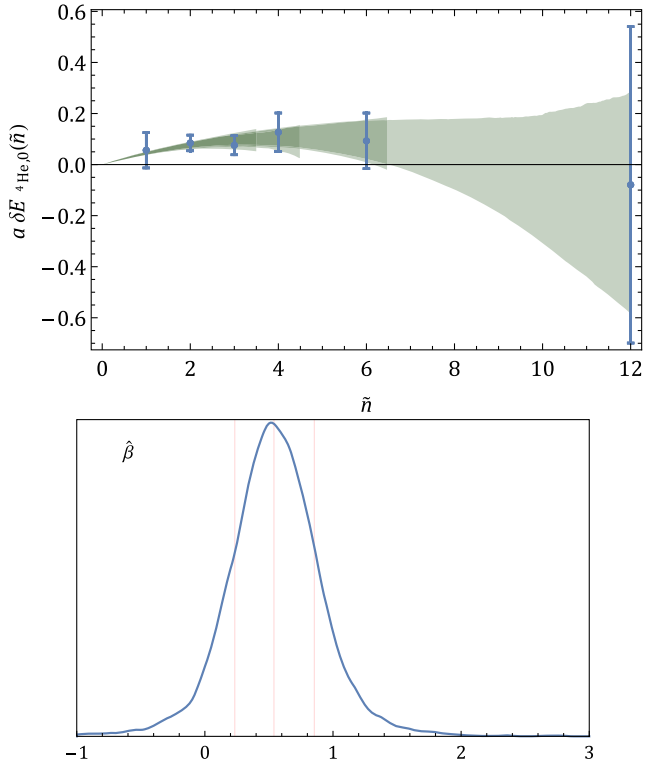

FIG. 19 (color online). Results for the energy shifts of ^{4}He as a function of the background magnetic field strength. The details of the figure are as in Fig. 10. The lower panel shows the PDF for the fit parameters $\hat{\beta}$.

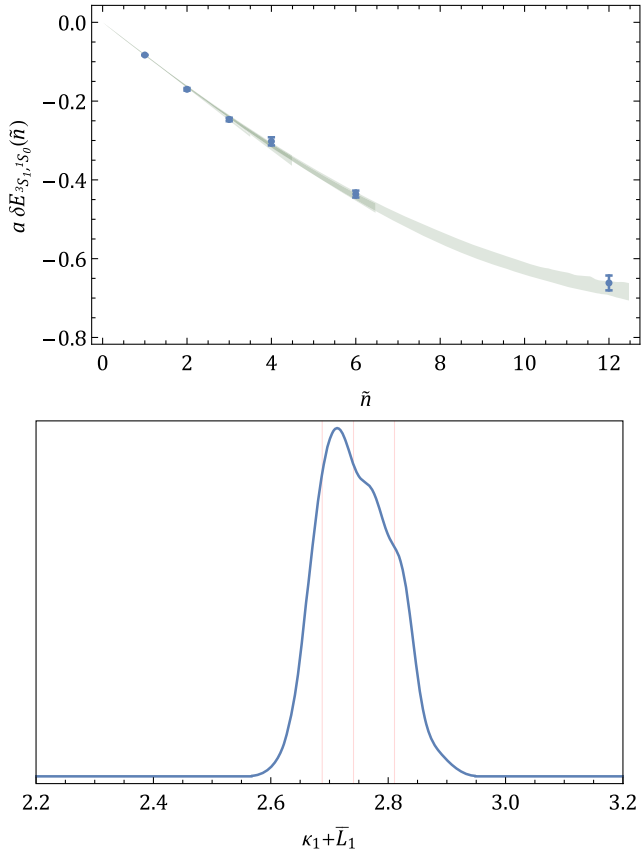

FIG. 20 (color online). Results for the differences in energy shifts between the two $j_z = I_z = 0$ np energy eigenstates as a function of the background magnetic field strength. The details of the figure are the same as in Fig. 10. The lower panel shows the PDF for the coefficient of the linear field dependence, $\kappa_1 + \bar{L}_1$.

by $B_{^4\mathrm{He}} = 107(24)$ MeV [34]. While it has no magnetic moment, it can be polarized by electromagnetic fields.

The EMPs obtained from ^{4}He correlation functions in the background magnetic fields are shown in Fig. 1, and the ratios of correlation functions are shown in Fig. 3, along with fits to their time dependence. The energy shifts extracted from fits to these ratios are given in Table I and are shown in Fig. 19. Analysis of the magnetic field strength dependence of the ^{4}He energies enables an extraction of the magnetic polarizability, giving

$$\hat{\beta}_{^4\mathrm{He}} = 0.54\begin{pmatrix}+0.32\\-0.31\end{pmatrix}(0.03). \tag{44}$$

E. The $j_z = I_z = 0$ np states and the $np \to d\gamma$ transition

The two energy eigenvalues of the coupled $j_z = I_z = 0$ np channels are shown in Fig. 6 for each magnetic field strength. To extract the $^3S_1$-$^1S_0$ mixing, and hence the short-distance two-nucleon (MEC) contribution to $np \to d\gamma$, the ratios of correlation functions $R_{^3S_1,^1S_0}(t;\mathbf{B})$ in Eq. (24) are constructed and shown in Fig. 7, along with fits to the time dependence. The energy shifts extracted from these ratios are shown in Fig. 20, along with the envelope of the ensemble of successful fits, from which the linear coefficient is found to be

$$\kappa_1 + \bar{L}_1 = 2.74\begin{pmatrix}+0.07\\-0.05\end{pmatrix}(0.07)\ \mathrm{nNM}, \tag{45}$$

where the result is presented in dimensionless units determined by the natural nuclear magneton at this pion mass. Fits of up to quadratic order are considered in this analysis.

To further isolate the short-distance two-nucleon contribution, the ratios $\delta R_{^3S_1,^1S_0}(t;\mathbf{B})$, defined in Eq. (25), are formed. By design, the energy shifts extracted from these ratios (see Fig. 8) have the form $2|e\mathbf{B}|\bar{L}_1/M + \mathcal{O}(|e\mathbf{B}|^2)$. These shifts are shown in Fig. 21, and performing polynomial fits to the dependence on the magnetic field strength leads to

$$\bar{L}_1 = 0.207\begin{pmatrix}+0.020\\-0.020\end{pmatrix}(0.006)\ \mathrm{nNM}. \tag{46}$$

Given the isovector magnetic moment and the short-distance two-nucleon contribution, the cross section for the process $np \to d\gamma$ can be determined near threshold at

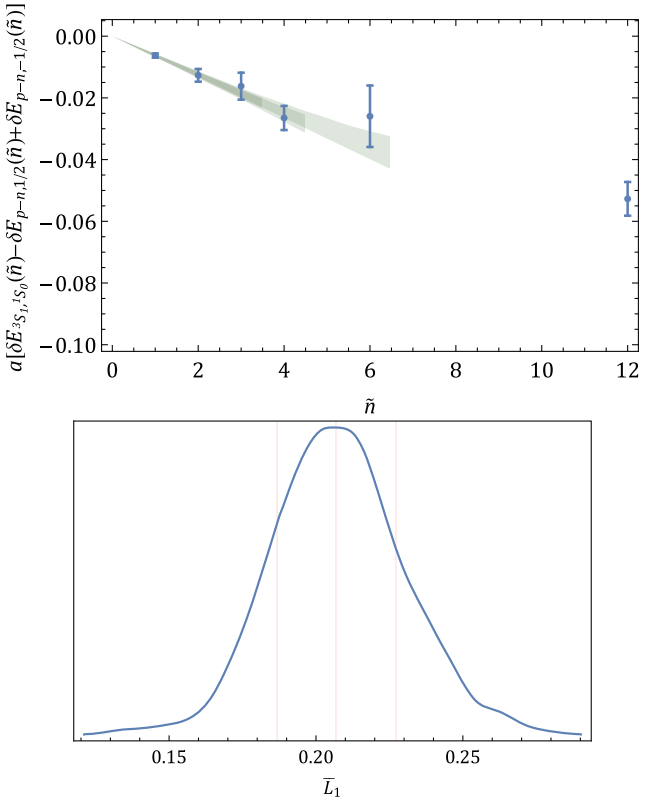

FIG. 21 (color online). The correlated difference between the differences in energy shifts between the two np $j_z = 0$ energy eigenstates and those of the isovector nucleon [see Eq. (25)] as a function of the background magnetic field strength. The details of the figure are the same as in Fig. 10.

$m_\pi \sim 806$ MeV. Even though the LQCD calculations determine these parameters from mixing between bound states, the EFT($\not\pi$) framework is valid for low-energy scattering states and can be immediately applied. It is conventional to use a multipole expansion to define the cross section for the radiative-capture process $np \to d\gamma$ at low energies [63,75,76],

$$\sigma(np \to d\gamma) = \frac{e^2(\gamma_0^2 + |\mathbf{p}|^2)^3}{M_N^4 \gamma_0^3 |\mathbf{p}|}[|\tilde{X}_{M1}|^2 + |\tilde{X}_{E1}|^2 + \cdots], \tag{47}$$

where $\tilde{X}_{M1}$ is the $M1$ amplitude and $\tilde{X}_{E1}$ is the $E1$ amplitude for the process, γ_0 is the binding momentum of the deuteron, and $\mathbf{p}$ is the momentum of each incoming nucleon in the center-of-mass frame. The ellipsis denotes higher-order amplitudes, suppressed by powers of the photon momentum. Following Refs. [64,65], it is straightforward to show that the amplitudes at NLO, with the dibaryon parametrization of Eq. (15), are

$$\tilde{X}_{E1} = -\frac{1}{\sqrt{1-\gamma_0 r_3}} \frac{|\mathbf{p}| M_N \gamma_0^2}{(|\mathbf{p}|^2 + \gamma_0^2)^2},$$
$$\tilde{X}_{M1} = \frac{Z_d}{-\frac{1}{a_1} + \frac{1}{2} r_1 |\mathbf{p}|^2 - i|\mathbf{p}|} \times \left[\frac{\kappa_1 \gamma_0^2}{\gamma_0^2 + |\mathbf{p}|^2}\left(\gamma_0 - \frac{1}{a_1} + \frac{1}{2} r_1 |\mathbf{p}|^2\right) + \frac{\gamma_0^2}{2} l_1\right], \tag{48}$$

where the quantities appearing in this expression are defined in Sec. III B. Near threshold, the $E1$ amplitude is subleading and will be ignored. Inserting the extracted values for κ_1, $\bar{L}_1$, the binding energy from Ref. [34], and the scattering lengths and effective ranges from Ref. [35] leads to a radiative capture cross section at the SU(3) symmetric point of

$$\sigma(np \to d\gamma)|_{m_\pi \sim 806\ \text{MeV}} = 17 \begin{pmatrix} +101 \\ -16 \end{pmatrix} \text{ mb}, \tag{49}$$

for an incident neutron speed of $v = 2200$ m/s, accurate up to NLO in EFT($\not\pi$). Because of the nonlinear nature of the dependence of the cross section on the inputs, the distribution is extremely non-Gaussian; the central value is reported as the 50th quantile and the uncertainty bounds as the 17th and 83rd quantiles of the full distribution. Improving on this uncertainty requires significantly better determinations of the scattering parameters and the binding momentum. At the physical point, the cross section is known to be $\sigma(np \to d\gamma) = 334.2(0.5)$ mb [77] at this relative velocity, which is significantly larger. The short-distance two-body contribution in the calculated cross section [Eq. (49)] is about 10%, just as in the phenomenological determinations. Accounting for the significantly different phase space available at the SU(3) point, and the greatly different scattering parameters in both channels, the discrepancy in the cross section is unsurprising. In Ref. [30], this result is combined with an analogous result at $m_\pi \sim 450$ MeV to extrapolate to the physical point and postdict a cross section of $\sigma^{\text{lqcd}}(np \to d\gamma) = 332.4(^{+5.4}_{-4.7})$ mb.

IV. SUMMARY

The magnetic moments and magnetic polarizabilities of the lightest few nuclei have been calculated at a pion mass of $m_\pi \sim 806$ MeV using LQCD in the presence of background magnetic fields. In addition, by considering the mixing of two-nucleon states with $j_z = I_z = 0$, the $\bar{L}_1$ counterterm of EFT($\not\pi$) that governs short-distance two-nucleon contributions to the radiative-capture process $np \to d\gamma$ has been determined. This has then been used to predict the near threshold capture cross section at this pion mass. The success of the calculations presented in this

TABLE II. The results of our previous calculations of the nucleon and nuclear magnetic moments [29] from spin splittings at a pion mass of $m_\pi \sim 806$ MeV. The first uncertainty is statistical while the second is the complete systematic. As discussed in the text, these values are more precise than those determined from the more complex analysis required to extract the polarizabilities.

State	μ[nNM]
n	$-1.981(05)(18)$
p	$+3.119(33)(64)$
$d(j_z = \pm 1)$	$+1.218(38)(87)$
^{3}He	$-2.29(03)(12)$
^{3}H	$+3.56(05)(18)$

work, and in Refs. [29,30], demonstrate the feasibility of studying the structure of nuclei directly from QCD and open the way to a variety of additional QCD calculations of the structure and interactions of light nuclei.

The LQCD calculations have been performed at a single lattice spacing and in one lattice volume, and the lack of continuum and infinite-volume extrapolations introduces systematic uncertainties into the results. The effects of the FV used in this work on the binding energies of the light nuclei have been explicitly quantified in previous works [34] and found to be small. It is expected that such effects in the moments and polarizabilities are of comparable size. An additional uncertainty of $e^{-\gamma L}$ is assigned to the extracted values of nuclear moments and polarizabilities, and for simplicity, we conservatively use $\gamma = \gamma_d \sim 190$ MeV for the binding momentum, leading to a $\sim$3% uncertainty. For the single nucleons, the expected volume effects of $\mathcal{O}(e^{-m_\pi L})$ are negligibly small. Calculations with multiple lattice spacings have not been performed, and this systematic uncertainty remains to be quantified. The electromagnetic contributions to the action are perturbatively improved as they are included as a background field in the link variables. Therefore, the lattice-spacing artifacts are expected to be small, appearing at $\mathcal{O}(\Lambda_{\rm QCD}^2 a^2, \alpha^2 \Lambda_{\rm QCD} a) \sim 3\%$ for $\Lambda_{\rm QCD} = 300$ MeV. To account for these effects in dimensionless quantities, an overall multiplicative systematic uncertainty of 3% is assigned to the extracted magnetic moments and $\bar{L}_1$, and an uncertainty of 5% is assessed on all of the polarizabilities, where more complicated effects that compound these uncertainties may be possible. For nuclei, these contributions are small compared to the other systematic uncertainties. The main results are presented in terms of dimensionless quantities, but in Table III, we also convert the polarizabilities to physical units using the lattice spacing $a = 0.110(1)$; since the units of polarizabilities are fm^3, the scale-setting uncertainty corresponds to an additional 3% uncertainty that is added in quadrature. Unfortunately, the calculations of the individual polarizabilities are incomplete because of the omission of the disconnected contributions (the coupling of the external field to the sea quarks); however, empirical evidence [47,52,53] suggests that the omitted contributions will lead to only small modifications that lie within the current uncertainties. Confirming this expectation is left to future work. We stress that the magnetic moments and the $M1$ transition amplitude for $np \to d\gamma$ are not afflicted by the absence of disconnected diagrams [and neither are isovector differences such as $\beta_p - \beta_n$ at the SU(3) point].

The magnetic moments and polarizabilities that have been determined in this work and in Ref. [29] are summarized in Tables II and III and are shown in Figs. 22 and 23 (the magnetic moments calculated from spin splittings in Ref. [29] are the most precise determinations). The electrically neutral systems are found to be by far the most precise because the electrically charged systems are defined by Landau levels, which have less than ideal overlap with the interpolating operators used to form the correlation functions.

These results, while not obtained at the physical values of the light-quark masses, are interesting in their own right

TABLE III. The magnetic polarizabilities calculated in this work at a pion mass of $m_\pi \sim 806$ MeV. An additional 5% uncertainty is associated with each polarizability as an estimate of discretization and finite volume effects. For the polarizabilities presented in physical units, an additional scale setting systematic uncertainty (3%) is included in quadrature in the second uncertainty.

State	$\hat{\beta} = M_N^2 (M_\Delta - M_N)/e^2 \times \beta$	β [10^{-4} fm^3]
n	$0.198(^{+0.009}_{-0.011})(0.010)$	$1.253(^{+0.056}_{-0.067})(0.055)$
p	$0.83(^{+0.10}_{-0.07})(0.04)$	$5.22(^{+0.66}_{-0.45})(0.23)$
nn	$0.296(^{+0.019}_{-0.018})(0.015)$	$1.872(^{+0.121}_{-0.113})(0.082)$
pp	$0.84(^{+0.41}_{-0.36})(0.04)$	$5.31(^{+2.59}_{-2.27})(0.23)$
$d(j_z = \pm 1)$	$0.70(^{+0.24}_{-0.23})(0.04)$	$4.4(^{+1.6}_{-1.5})(0.2)$
^{3}He	$0.85(^{+0.34}_{-0.32})(0.04)$	$5.4(^{+2.2}_{-2.1})(0.2)$
^{3}H	$0.40(^{+0.27}_{-0.27})(0.02)$	2.6(1.7)(0.1)
^{4}He	$0.54(^{+0.32}_{-0.31})(0.03)$	$3.4(^{+2.0}_{-1.9})(0.2)$

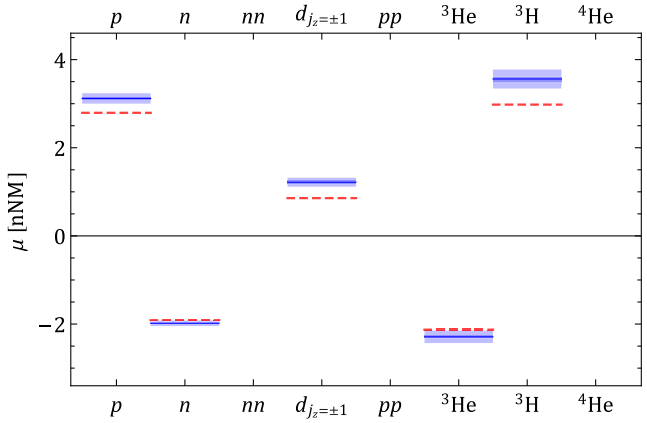

FIG. 22 (color online). A summary of the magnetic moments of the nucleons and light nuclei calculated with LQCD at SU(3) symmetric quark masses corresponding to a pion mass of $m_\pi \sim 806$ MeV. The results are presented in units of natural nuclear magnetons. The red dashed lines correspond to the experimental magnetic moments.

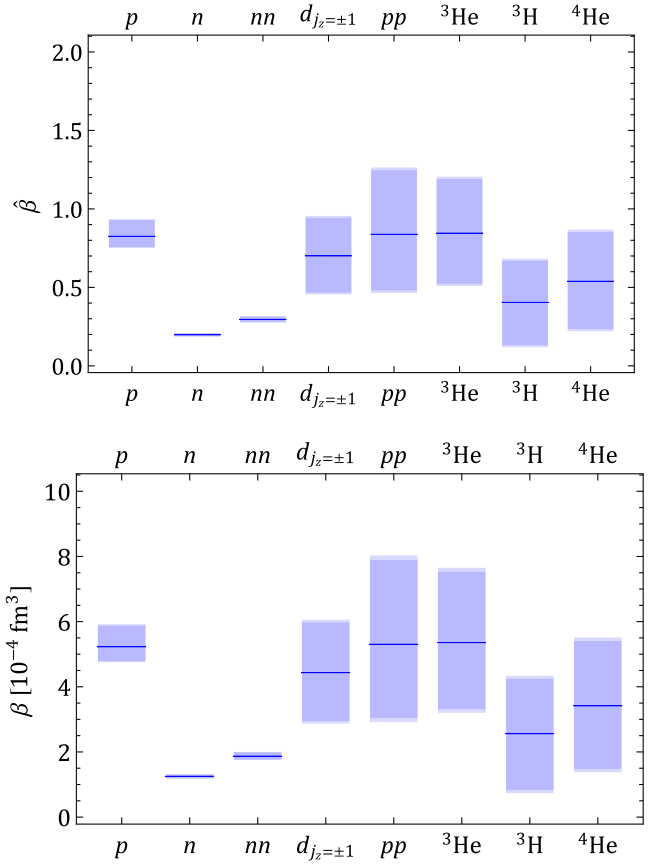

FIG. 23 (color online). A summary of the magnetic polarizabilities of the nucleons and light nuclei calculated with LQCD at a pion mass of $m_\pi \sim 806$ MeV. The upper panel presents the dimensionless quantity $\hat{\beta} = M_N^2(M_\Delta - M_N)\beta/e^2$ obtained from the fits with the inner shaded region representing the total uncertainty arising from statistical and fitting systematic uncertainties. The outer shaded region assesses additional systematic uncertainties from discretization effects and FV effects, combined in quadrature and applied multiplicatively. The lower panel presents the polarizabilities in physical units; in this case, the outer shaded region also includes the effect of the scale setting uncertainty.

and suggest important features of these systems. First, our calculations are sufficiently precise to determine that the strong interactions between neutrons are such that when placed into a magnetic field, the two-neutron system is more magnetically rigid than the sum of the individual neutrons. This is consistent with expectations at the physical quark masses based upon phenomenological nuclear interactions [78], and indicates that it is energetically disfavored for a neutron star to lower its energy by spontaneously generating a large magnetic field. Second, a large isovector component to the nucleon magnetic polarizability is found. The proton polarizability is found to be considerably larger than that in nature while the neutron polarizability is consistent with the phenomenological value, but much more precise. Third, analysis of the $j_z = I_z = 0$ np system leads to a precise extraction of the coefficient, $\tilde{L}_1$, of the short-distance two-body magnetic current operator connecting the $^3S_1$ and $^1S_0$ states in the context of EFT($\not\pi$). This operator provides an important contribution to the $np \to d\gamma$ capture cross section near threshold, which is a critical input for calculations of the production of elements in big-bang nucleosynthesis and in other environments as is discussed further in Ref. [30].

These calculations are the first of their kind and are the initial steps in a comprehensive program to determine the electromagnetic properties of the light nuclei as well as the response of nuclei to electroweak currents. The next steps will include calculations of axial matrix elements in the various light nuclei, as these are of significant phenomenological interest in neutrino-nucleus scattering experiments. Further, this points the way to calculating matrix elements of interactions required in laboratory searches for dark matter and other potential beyond the Standard Model scenarios which involve nuclear matrix elements of a variety of currents. Calculations at smaller lattice spacings and in other volumes, as well as for lighter quark masses where direct connection to experiment can be made are important to this program. Finally it is important to include the presently omitted couplings of sea quarks to the background fields. Calculations addressing these goals are planned for the future.

ACKNOWLEDGMENTS

We would like to thank Zohreh Davoudi, Harald Grießhammer, Daekyoung Kang, David B. Kaplan, Daniel Phillips, and Sanjay Reddy for several interesting discussions, and in particular Zohreh Davoudi for

exchanges leading to clarifications of the Appendix. Calculations were performed using computational resources provided by the Extreme Science and Engineering Discovery Environment (XSEDE), which is supported by National Science Foundation Grant No. OCI-1053575, NERSC (supported by U.S. Department of Energy Grant No. DE-AC02-05CH11231), and by the USQCD Collaboration. This research used resources of the Oak Ridge Leadership Computing Facility at the Oak Ridge National Laboratory, which is supported by the Office of Science of the U.S. Department of Energy under Contract No. DE-AC05-00OR22725. The PRACE Research Infrastructure resources Curie based in France at the Très Grand Centre de Calcul and MareNostrum-III based in Spain at the Barcelona Supercomputing Center were also used. Parts of the calculations used the Chroma software suite [79]. S. R. B. was partially supported by NSF continuing Grant No. PHY1206498. W. D. was supported by the U.S. Department of Energy Early Career Research Award No. DE-SC0010495. K. O. was supported by the U.S. Department of Energy through Grant No. DE- FG02-04ER41302 and through Grant No. DE-AC05-06OR23177 under which JSA operates the Thomas Jefferson National Accelerator Facility. The work of A. P. was supported by Contract No. FIS2011-24154 from MEC (Spain) and FEDER. M. J. S. was supported by DOE Grant No. DE-FG02-00ER41132. B. C. T. was supported in part by a joint City College of New York-RIKEN/Brookhaven Research Center fellowship, a grant from the Professional Staff Congress of the CUNY, and by the U.S. National Science Foundation, under Grant No. PHY12-05778.

APPENDIX A: CHARGED-PARTICLE CORRELATION FUNCTIONS: SOURCE LOCATION AND GAUGE ORIGIN

1. General discussion

In addition to a uniform magnetic field, the Abelian gauge links in Eq. (2) lead to two further gauge-invariant quantities that are finite volume artifacts. These quantities are the Wilson loops $W_1(x_2)$ and $W_2(x_1)$ appearing in Eq. (3), which express the nonvanishing holonomies of the background gauge field. A major consequence of these nonvanishing holonomies is the breaking of discrete translational invariance down to a smaller subgroup, which is referred to as the magnetic translation group; see Ref. [80]. The size of this subgroup depends on the magnetic-flux quantum, $\tilde{n}$, as

$$W_1\left(x_2+\frac{j}{3q_q\tilde{n}}L\right)=W_1(x_2),\quad \text{and}$$
$$W_2\left(x_1+\frac{j}{3q_q\tilde{n}}L\right)=W_2(x_1), \tag{A1}$$

for $j=0,1,\ldots,3|q_q|\tilde{n}-1$. Consequently lattice translational invariance for down-type quarks coupled to $U_\mu^{(Q)}(x)$, for example, is reduced to $\mathbb{Z}_{\tilde{n}}\times\mathbb{Z}_{\tilde{n}}\times\mathbb{Z}_{\frac{L}{a}}$. This is to be contrasted with the infinite-volume case, where full translational invariance in a uniform magnetic field is maintained due to gauge invariance. On a torus, gauge invariance is more restrictive due to the additional specification of Wilson loops, and translational invariance is consequently reduced.

For charged-particle correlation functions, the reduced translational invariance can lead to subtle effects. For example, consider electromagnetic gauge links that are unity at the origin, $U_\mu^{(Q)}(0)=1$, such as those in Eq. (2), and the hadronic source to be at the spatial position $\boldsymbol{x}_i$. The electromagnetic gauge links can be altered so that they become unity at the source location; however, this cannot be achieved by a gauge transformation because the Wilson loops would be modified by[13]

$$W_1(x_2)\to W_1(x_2)W_1^\dagger(x_{i,2}),\quad \text{and}$$
$$W_2(x_1)\to W_2(x_1)W_2^\dagger(x_{i,1}). \tag{A2}$$

Similarly, translational invariance cannot be used to relocate the hadronic source to the origin without altering the correlation function. Consequently charged-particle correlation functions depend on the origin of the gauge potential, and the location of the source. Even when $\boldsymbol{x}_i$ is related to the origin of the gauge potential by a discrete magnetic translation, which corresponds to the special case where the required translation is equivalent to a gauge transformation, the charged-particle correlation function will not be identical due to gauge dependence.[14] As the degree to which lattice translational invariance is reduced depends on the strength of the magnetic field, steps are required to ameliorate this situation.

[13]The electromagnetic gauge links are accordingly modified in the form $U_\mu^{(Q)}(x)\to U_\mu^{(Q)}[(x-x_i)\mathrm{mod}\frac{L}{a}]$. The new links $U_\mu^{(Q)}[(x-x_i)\mathrm{mod}\frac{L}{a}]$ are related to $U_\mu^{(Q)}(x-x_i)$ through a gauge transformation; however, such a transformation alters the functional dependence of charged-particle correlation functions. Because the Wilson loops are gauge invariant, there is no difference, for example, between $W_1[(x_2-x_{i,2})\mathrm{mod}\frac{L}{a}]$ and $W_1(x_2-x_{i,2})=W_1(x_2)W_1^\dagger(x_{i,2})$, which appears above.

[14]The definition of the charged particle two-point function could be altered to include an electromagnetic gauge link between the source and sink locations. The resulting correlation functions would be gauge invariant; but, the cost is the introduction of a path for the gauge link. Because magnetic flux threads closed loops that are oriented transverse to the magnetic field, the resulting correlation function is then path dependent.

One way to deal with the problem is to fix the background field entirely including the holonomies. This approach can be implemented by randomly choosing a source location before including the $U_\mu^{(Q)}(x)$ links. The hadron source location must still be chosen relative to the gauge potential, and a convenient choice is to make them coincident. This method does not introduce constant shifts of the gauge holonomy and was employed in [43] to investigate magnetic properties of the nucleon. The choice of a coincident location, however, is not required; and other choices for the relative separation that are not related by a magnetic translation could be averaged over to mitigate FV effects.

An alternative approach to reduce FV effects consists of varying the holonomies. One way to achieve this consists of introducing a constant shift in the gauge potential, which is equivalent (after field redefinition) to implementing twisted boundary conditions (BCs) on the quarks.[15] These are flavor dependent BCs due to the difference in quark electric charges. Ultimately to remove the arbitrariness of this choice, all nonequivalent shifts should be averaged over. The resulting twist average removes the FV effect associated with translational invariance, and related proposals have recently been suggested more generally to reduce FV effects in other lattice QCD computations [81,82].[16]

The present calculations were performed with the following approach to handle the lack of lattice translational invariance. The source locations were varied relative to the origin of the gauge potential, rather than varying the gauge holonomies. Varying the source locations allows for the restoration of lattice translational invariance in two equivalent ways: averaging over all sources on a given configuration, and then performing the ensemble average; or performing the ensemble average with a fixed source location, and then averaging over all locations. In this work, a hybrid approach was chosen because of limited computational resources. Each QCD gauge configuration was postmultiplied by the Abelian gauge links $U_\mu^{(Q)}(x)$, and then a random offset was introduced. The random offset was the same for each value of the magnetic flux quantum, $\tilde{n}$, in order to maximize correlations between differing field strengths. On each configuration, quark propagators were calculated using 48 symmetrically distributed source locations. In addition to improving statistics, the source averaging partially restores lattice translational invariance on each configuration. Translational invariance is further improved in the ensemble average, because a random offset is chosen for each configuration.

While quark propagators are subject to finite-size effects owing to the reduction in translational invariance, hadronic correlation functions for neutral particles are less susceptible. Using the neutron as an example, the nonvanishing holonomies of the gauge field show up only in exponentially small FV corrections to the neutron energy [84]. These corrections arise primarily from charged pion fluctuations that wind around the torus. For charged particles, however, the reduction in translational invariance has a direct effect on the coordinate dependence of their correlation functions. In turn, the overlap of a given hadronic interpolating field onto Landau levels depends on the hadron source location and gauge holonomy in a field-dependent way. To make this discussion more concrete, the simplified case of a pointlike charged particle subject to the same method utilized in the present LQCD calculation is explored.

2. Expectations for a pointlike charged particle

To illustrate the dependence of charged particle correlation functions on the source location and gauge holonomy, a pointlike particle propagating in an external magnetic field on a torus is considered. In the pointlike approximation, the spin-projected hadron propagator can be derived following the arguments in [56,84]. Various ways to reduce finite-size effects by shifting the gauge potential and/or shifting the source location are considered.

In practice, the pointlike approximation is valid only when the typical hadronic size cannot be resolved in a given Landau level. For example, higher-lying Landau levels have a larger (rms) radius, $\propto \sqrt{(n_L+\frac{1}{2})/|Q_h eB|}$; hence, the details of the hadronic state will be less relevant compared with lower Landau levels. By contrast, the lowest Landau level is the most sensitive to hadron structure, and the most likely to be dynamically altered away from the pointlike result. With magnetic fields that are not arbitrarily weak, more dependence on hadronic structure can be expected, and the pointlike particle case may thus only provide a guide. Further study is needed to address the dynamical Landau levels of bound states and to design better interpolating operators for hadrons in magnetic fields.

Employing a uniform shift of the gauge potential transverse to the magnetic field direction, the gauge links are modified to

[15]Shifting the source and shifting the gauge potential are equivalent up to a gauge transformation; however, this leads to different expectations for charged particle correlation functions, as shown below.

[16]In the analogous case of time-varying gauge potentials which lead to electric fields, a variant of this procedure was carried out for the neutron [83]. In that study, results at second order in the gauge potential, A_μ, were directly isolated by perturbatively expanding external field correlation functions, and enforcing temporal Dirichlet BCs. While twist averaging does not eliminate the FV effect in that case, it was shown that the neutron electric polarizability can nonetheless be separated from finite-size effects by efficacious shifts of the gauge potential.

$$U_1^{(Q)}(x) = \exp[-iq_q\theta_1 a/L] \times \begin{cases} 1 & \text{for } x_1 \neq L-a \\ \exp\left[-iq_q\tilde{n}\frac{6\pi x_2}{L}\right] & \text{for } x_1 = L-a \end{cases},$$
$$U_2^{(Q)}(x) = \exp[-iq_q\theta_2 a/L]\exp\left[iq_q\tilde{n}\frac{6\pi a x_1}{L^2}\right],$$
$$U_{3,4}^{(Q)}(x) = 1. \tag{A3}$$

To compute the propagator analytically for a charged quark propagating in the external gauge field specified by Eq. (A3), we find it convenient to perform a field redefinition on the quark field. The effect of this redefinition is to trade in the periodic fields for quarks with both magnetic periodic and twisted boundary conditions [which, for simplicity, we term magnetic-twisted BCs; see Eq. (A8)], and links that are periodic up to a gauge transformation. The propagator for a structureless charged particle then has the form

$$C_{h,j_z}(x,x_i;\boldsymbol{\theta},\boldsymbol{B}) = \sum_{\boldsymbol{\nu}} e^{-iQ_h\boldsymbol{\theta}\cdot\boldsymbol{\nu}_\perp}[W_2^\dagger(x_1)]^{\nu_2} C_{h,j_z}^{(\infty)}(x+\boldsymbol{\nu}L,x_i;\boldsymbol{B}), \tag{A4}$$

where x and x_i are the spacetime locations of the sink and source relative to the origin, respectively, and $\boldsymbol{\nu}$ is a triplet of integers. Images transverse to the magnetic field direction, $\boldsymbol{\nu}_\perp = (\nu_1,\nu_2)$, pick up phases arising from the constant shift of the gauge potential. Notice the Euclidean time direction is treated as infinite in extent. The propagator $C_{h,j_z}^{(\infty)}(x,x_i;\boldsymbol{B})$ is that for a charged particle in infinite volume. Ignoring discretization effects, the continuum form of the infinite volume propagator is employed, which in coordinate space is [84]

$$C_{h,j_z}^{(\infty)}(x,x_i;\boldsymbol{B}) = \mathfrak{W}^\dagger(x,x_i)\mathfrak{C}_{h,j_z}^{(\infty)}(x-x_i;\boldsymbol{B}), \tag{A5}$$

and consists of two parts. There is a spacetime translationally invariant part

$$\mathfrak{C}_{h,j_z}^{(\infty)}(z;\boldsymbol{B}) = \int_0^\infty \frac{ds}{(4\pi s)^2}\frac{Q_h eBs}{\sinh(Q_h eBs)} \times \exp\left\{-s\tilde{E}_{h,j_z}^2 - \frac{Q_h eB}{4\tanh(Q_h eBs)} \times [z_1^2+z_2^2] - \frac{1}{4s}[z_3^2+z_4^2]\right\}, \tag{A6}$$

which contains the hadron energy $\tilde{E}_{h,j_z}$ appearing in Eq. (7); however, the tilde denotes that it excludes the contribution to the energy from the n_Lth Landau level. Instead, contributions from all Landau levels are contained in this propagator [85]. The remaining part $\mathfrak{W}^\dagger(x,x_i)$ is not translationally invariant and accordingly depends on the gauge. It can be written as a Wilson line evaluated on the straight-line path[17] between x_i and x,

$$\mathfrak{W}(x,x_i) = \exp\left[iQ_h e\int_{x_i}^{x} dz_\mu A_\mu(z)\right] = \exp\left[-\frac{i}{2}Q_h eB(x_1-x_{i,1})(x_2+x_{i,2})\right]. \tag{A7}$$

In writing the FV propagator in Eq. (A4), the Wilson loops have been implicitly modified to include the hadron's electric charge, $Q_h e$, instead of the quark charge, $q_q e$, and the charged hadron propagator $C_{h,j_z}(x,x_i;\boldsymbol{\theta},\boldsymbol{B})$ satisfies the following BCs in the directions transverse to the magnetic field:

$$C_{h,j_z}(x+L\hat{x}_1,x_i;\boldsymbol{\theta},\boldsymbol{B}) = e^{iQ_h\theta_1}C_{h,j_z}(x,x_i;\boldsymbol{\theta},\boldsymbol{B}),$$
$$C_{h,j_z}(x+L\hat{x}_2,x_i;\boldsymbol{\theta},\boldsymbol{B}) = e^{iQ_h\theta_2}W_2(x_1)C_{h,j_z}(x,x_i;\boldsymbol{\theta},\boldsymbol{B}). \tag{A8}$$

The first is a twisted BC, while the second emerges as a magnetic-twisted BC. In the actual computation, periodic quark propagators are calculated using the gauge links in Eq. (A3). The quark field redefinition leads to the BCs in Eq. (A8). Because of the gauge shift, the gauge potential no longer vanishes at the origin; e.g., the links $U_2^{(Q)}(x)$ are unity when $x_1 = \theta_2 L/6\pi\tilde{n}$. Finally, notice the asymmetric appearance of the holonomy $W_2(x_1)$ in Eq. (A4). The Wilson loop $W_1(x_2)$ does not appear explicitly in the sum over the winding number ν_1, and the charged-particle propagator is twisted in the x_1-direction rather than magnetic twisted; see Eq. (A8). The effect of this Wilson loop, however, is contained implicitly in the sum over winding number ν_1 because of the x_2-coordinate dependence of the Wilson line $\mathfrak{W}(x,x_i)$. This asymmetry in the charged-particle propagator and the BCs that result from it are directly related to the asymmetric choice of gauge.

Given the form of the propagator in Eq. (A4), a natural question to ask is whether shifting both the gauge potential and the source location is superfluous. To answer this question, one can express the propagator in terms of the source-sink separation, $\Delta\boldsymbol{x} = \boldsymbol{x} - \boldsymbol{x}_i$, and attempt to absorb the remaining dependence on the source location into a redefinition of the twist angles $\boldsymbol{\theta}$. Because of the breaking of translational invariance, this is not possible. By virtue of the Wilson line $\mathfrak{W}(x,x_i)$, the correlation function retains explicit dependence on $x_{i,2}$, which is measured relative to the origin. The origin has no significance for gauge-invariant quantities; however, in terms of the gauge links, the origin can readily be discerned [see Eq. (A3)]. As a consequence, gauge variant quantities, such as the charged-particle propagator, can depend on positions relative to the origin.

[17]While the straight-line path is not the only path that can be chosen for the Wilson line, the choice of path is not completely arbitrary with $\mathfrak{W}(x,x_i)$ implemented as in Eq. (A7) [85].

Four scenarios are considered, denoted by Γ: (i) periodic BCs with coincident origins of the gauge potential and source for the correlation functions ($\Gamma = 0$), (ii) shifting the gauge potential ($\Gamma = \boldsymbol{\theta}$), (iii) shifting the source location ($\Gamma = X$), and (iv) varying the shift in the gauge potential and shifting the source location ($\Gamma = \boldsymbol{\theta}X$).

a. Periodic BCs with coincident origins ($\Gamma = \mathbf{0}$)

Choosing the origin of the gauge potential to coincide with that of the source and not including a uniform gauge field corresponds to specifying $\boldsymbol{x}_i = \mathbf{0}$, and $\boldsymbol{\theta} = \mathbf{0}$. The latter leads to periodic quarks (up to a gauge transformation). This method was chosen in [43]. Additionally in that study, as in this work too, the spatial sink location is summed over, which projects the correlator onto vanishing three-momentum. Three-momentum states do not have definite energy eigenvalues, however, and one expects correlation functions to contain multiple low-lying Landau levels. For a pointlike particle on a continuous torus, consider the spatially integrated correlation function,

$$C_0(t) = \int_0^L d\boldsymbol{x} C_{h,j_z}(x, 0; \mathbf{0}, \boldsymbol{B}). \tag{A9}$$

Carrying out the three-momentum projection gives

$$C_0(t) = \frac{1}{2}\int_0^\infty \frac{ds}{\sqrt{2\pi s}} e^{-\frac{1}{2}s\tilde{E}^2_{h,j_z} - \frac{1}{4s}t^2} \times \int_0^L dx_2 \sum_{\nu_2=-\infty}^{\infty} \langle x_2, s | \nu_2 L, 0\rangle, \tag{A10}$$

which has been written in terms of the quantum-mechanical propagator for the simple harmonic oscillator

$$\langle x', t' | x, t\rangle = \theta(t'-t)\sqrt{\frac{Q_h eB}{2\pi \sinh[Q_h eB(t'-t)]}} \times \exp\left\{-\frac{Q_h eB}{2\sinh[Q_h eB(t'-t)]} \times [(x'^2 + x^2)\cosh[Q_h eB(t'-t)] - 2x'x]\right\}, \tag{A11}$$

where t and t' are Euclidean times. In terms of Landau levels, the correlation function can be written as

$$C_0(t) = \sum_{n_L=0}^{\infty} Z^{(0)}_{n_L} \frac{e^{-E_{h,j_z}t}}{2E_{h,j_z}}, \tag{A12}$$

where the energies E_{h,j_z} include the Landau energy and are given in Eq. (7). The dimensionless coefficients $Z^{(0)}_{n_L}$ are given by

$$Z^{(0)}_{n_L} = \int_0^L dx_2 \psi^*_{n_L}(x_2) \sum_{\nu_2=-\infty}^{\infty} \psi_{n_L}(\nu_2 L), \tag{A13}$$

and are written in terms of the coordinate wave functions, which have the standard form in terms of Hermite polynomials

$$\psi_{n_L}(x) = \frac{1}{\sqrt{2^{n_L} n_L! \sqrt{\frac{\pi}{|Q_h eB|}}}} H_{n_L}(\sqrt{|Q_h eB|}x) e^{-\frac{1}{2}|Q_h eB|x^2}. \tag{A14}$$

Notice that contributions from odd-parity Landau levels are absent due to the sum over winding number. The coefficients $Z^{(0)}_{n_L}$ are not positive; spectral positivity is not maintained due to the lack of translational invariance. For quantized values of the magnetic field, these coefficients depend on the flux quantum $\tilde{n}$, but not on the size L. This dependence on $\tilde{n}$, however, is exponentially suppressed.

b. Shifting the gauge potential ($\Gamma = \boldsymbol{\theta}$)

While shifting the gauge potential has not been pursued as a means to reduce FV effects, it is instructive to discuss briefly pointlike expectations for this method. Averaging over all possible shifts of the gauge potential is equivalent to averaging over quarks with randomly twisted boundary conditions. As a result, the twist-averaged propagator in Eq. (A4) receives contributions only from zero winding numbers $\boldsymbol{\nu}_\perp = \mathbf{0}$. While this is a desirable feature, there is no further simplification of the charged particle correlation function. The twists can be utilized, however, to form the infinite volume propagator via constructing the Fourier transformation in blocks [82]. The lack of lattice translational invariance means that the magnetic periodic images, rather than periodic images, must be summed over. In effect, this provides access to $C^{(\infty)}_{h,j_z}(x, x_i; \boldsymbol{B})$, for $\vec{x}_\perp$ over the whole transverse plane. The resulting zero-momentum correlation function has the form

$$C_\theta(t) = \frac{1}{2}\int_0^\infty ds \frac{e^{-\frac{1}{2}s\tilde{E}^2_{h,j_z} - \frac{1}{4s}t^2}}{\sqrt{2\pi s}} \int_{-\infty}^{\infty} dx_2 \langle x_2, s | x_{i,2}, 0\rangle. \tag{A15}$$

In terms of Landau levels, the expected behavior is thus

$$C_\theta(t) = \sum_{n_L=0}^{\infty} Z^{(\theta)}_{n_L} \frac{e^{-E_{h,j_z}t}}{2E_{h,j_z}}, \tag{A16}$$

where the coefficients are given by

$$Z_{n_L}^{(\theta)} = \int_{-\infty}^{\infty} dx_2 \psi_{n_L}^*(x_2)\psi_{n_L}(x_{i,2}), \tag{A17}$$

in which there is no remaining dependence on L. When the source is located at the origin, there is no dependence on the magnetic flux quantum, $\tilde{n}$. Notice that there are no contributions from odd-parity Landau levels, and further that spectral positivity does not emerge.

c. Shifting the source location ($\Gamma = X$)

As described previously, source-to-all propagators are calculated in the present LQCD calculation, with sources randomly located relative to the gauge origin. A constant shift of the gauge potential is not implemented, and thus $\boldsymbol{\theta} = \mathbf{0}$, but with an approximate average over $\boldsymbol{x}_i$. This leads to the following expression for the correlation function of a pointlike charged particle,

$$C_X(t) = \frac{1}{2}\int_0^\infty ds \frac{e^{-\frac{1}{2}s\tilde{E}_{h,j_z}^2 - \frac{1}{4s}t^2}}{\sqrt{2\pi s}} \int_0^L dx_2 \times \int_0^L \frac{dx_{i,2}}{L} \langle x_2, s | x_{i,2}, 0\rangle. \tag{A18}$$

Performing the integration over source location $x_{i,1}$ restricted the winding number expansion to the sector with $\nu_2 = 0$. Using the spectral decomposition for the quantum-mechanical harmonic-oscillator propagator gives

$$C_X(t) = \sum_{n_L=0}^{\infty} Z_{n_L}^{(X)} \frac{e^{-E_{h,j_z}t}}{2E_{h,j_z}}, \tag{A19}$$

where E_{h,j_z} includes the energy of the n_Lth Landau level. The corresponding spectral weights are

$$Z_{n_L}^{(X)} = \frac{1}{L}\left|\int_0^L dx \psi_{n_L}(x)\right|^2, \tag{A20}$$

and give the probability of finding the charged particle in the n_Lth Landau level. Positivity of these weights arises due to the symmetric treatment of the source and sink locations. Landau levels of both parities contribute to the correlation function. When evaluated for quantized magnetic fields, the weights only depend on the flux quantum $\tilde{n}$. Ratios of coefficients, however, depend on $\tilde{n}$ through exponentially small terms.

d. Varying the gauge shift and source location ($\Gamma = \theta X$)

Despite computational requirements, it remains worthwhile to consider averaging over the shift of the gauge potential and the source location. The former can be used to construct magnetic-periodic images and build the infinite-volume propagator in blocks. The result of this procedure leads to

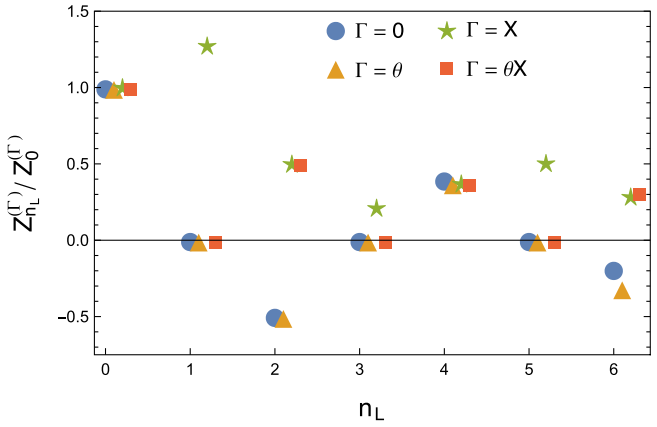

FIG. 24 (color online). Contributions to the correlation functions of a pointlike charged particle from the first few Landau levels compared with the contribution from the lowest Landau level. Four such coefficient ratios are considered, corresponding to different ways of dealing with the lack of lattice translational invariance, as described in the text. These are labeled by $\Gamma = 0, \theta, X$, and θX, which correspond to coincident origin, twist-averaged, source-averaged, and twist and source-averaged, respectively. Values have been slightly displaced in n_L to allow different ratios to be discernible. For quantized magnetic fields, all ratios are independent of the lattice size L, and ratios are either independent of the flux quantum $\tilde{n}$, or depend on it only through exponentially small terms.

$$C_{\theta X}(t) = \sum_{n_L=0}^{\infty} Z_{n_L}^{(\theta X)} \frac{e^{-E_{h,j_z}t}}{2E_{h,j_z}}, \tag{A21}$$

where E_{h,j_z} includes the energy of the n_Lth Landau level, and the corresponding spectral weights are

$$Z_{n_L}^{(\theta X)} = \frac{1}{L}\left|\int_{-\infty}^{\infty} dx \psi_{n_L}(x)\right|^2. \tag{A22}$$

This procedure eliminates all L dependence, and $\tilde{n}$ dependence is completely absent in ratios of coefficients. Furthermore, the procedure excludes contributions from odd-parity Landau levels and maintains spectral positivity.

3. Results for a pointlike particle

Having determined the charged-particle correlation functions for four different methods of dealing with the lack of translational invariance, the relative contributions of the lowest-lying Landau levels are compared in Fig. 24. In plotting the coefficient ratios, the n_L-dependence of the hadron energies E_{h,j_z} appearing in the correlation functions has been ignored. These energy denominators will lead to smaller coefficients, but only for higher-lying Landau levels.

[1] J.-W. Lee and B. C. Tiburzi, Phys. Rev. D **90**, 074036 (2014).
[2] F. Federspiel, R. Eisenstein, M. Lucas, B. MacGibbon, K. Mellendorf, A. Nathan, A. O'Neill, and D. Wells, Phys. Rev. Lett. **67**, 1511 (1991).
[3] A. Zieger, R. Van de Vyver, D. Christmann, A. De Graeve, C. Van den Abeele, and B. Ziegler, Phys. Lett. B **278**, 34 (1992).
[4] B. MacGibbon, G. Garino, M. Lucas, A. Nathan, G. Feldman, and B. Dolbilkin, Phys. Rev. C **52**, 2097 (1995).
[5] J. Beringer *et al.* (Particle Data Group), Phys. Rev. D **86**, 010001 (2012).
[6] L. Myers *et al.* (COMPTON@MAX-lab), Phys. Rev. Lett. **113**, 262506 (2014).
[7] V. Lensky and J. A. McGovern, Phys. Rev. C **89**, 032202 (2014).
[8] K. Kossert *et al.*, Eur. Phys. J. A **16**, 259 (2003).
[9] M. Lundin *et al.*, Phys. Rev. Lett. **90**, 192501 (2003).
[10] D. R. Phillips, J. Phys. G **36**, 104004 (2009).
[11] B. R. Holstein and S. Scherer, Annu. Rev. Nucl. Part. Sci. **64**, 51 (2014).
[12] M. N. Butler and M. J. Savage, Phys. Lett. B **294**, 369 (1992).
[13] M. N. Butler, M. J. Savage, and R. P. Springer, Nucl. Phys. **B399**, 69 (1993).
[14] W. Broniowski and T. D. Cohen, Phys. Rev. D **47**, 299 (1993).
[15] T. D. Cohen and W. Broniowski, Phys. Lett. B **292**, 5 (1992).
[16] V. Pascalutsa and D. R. Phillips, Phys. Rev. C **67**, 055202 (2003).
[17] H. W. Griesshammer, J. A. McGovern, and D. R. Phillips, arXiv:1509.09177.
[18] W. Detmold, B. Tiburzi, and A. Walker-Loud, Phys. Rev. D **73**, 114505 (2006).
[19] J.-W. Chen, H. W. Grießhammer, M. J. Savage, and R. P. Springer, Nucl. Phys. **A644**, 221 (1998).
[20] H. Grießhammer, J. McGovern, D. Phillips, and G. Feldman, Prog. Part. Nucl. Phys. **67**, 841 (2012).
[21] H. R. Weller, M. W. Ahmed, H. Gao, W. Tornow, Y. K. Wu, M. Gai, and R. Miskimen, Prog. Part. Nucl. Phys. **62**, 257 (2009).
[22] The MAX-IV Project, http://www.maxlab.lu.se/maxlab/max4/index.html (2011).
[23] E. Downie and H. Fonvieille, Eur. Phys. J. Spec. Top. **198**, 287 (2011).
[24] L. Myers, M. Ahmed, G. Feldman, S. Henshaw, M. Kovash, J. Mueller, and H. Weller, Phys. Rev. C **86**, 044614 (2012).
[25] L. Myers *et al.*, Phys. Rev. C **89**, 035202 (2014).
[26] L. Myers, M. Ahmed, G. Feldman, A. Kafkarkou, D. Kendellen, I. Mazumdar, J. Mueller, M. Sikora, H. Weller, and W. Zimmerman, Phys. Rev. C **C90**, 027603 (2014).
[27] D. Riska and G. Brown, Phys. Lett. B **38B**, 193 (1972).
[28] J. Hockert, D. Riska, M. Gari, and A. Huffman, Nucl. Phys. **A217**, 14 (1973).
[29] S. Beane, E. Chang, S. Cohen, W. Detmold, H. Lin, K. Orginos, A. Parreño, M. Savage, and B. Tiburzi, Phys. Rev. Lett. **113**, 252001 (2014).
[30] S. R. Beane, E. Chang, W. Detmold, K. Orginos, A. Parreño, M. Savage, and B. Tiburzi, Phys. Rev. Lett. **115**, 132001 (2015).
[31] M. Lüscher and P. Weisz, Commun. Math. Phys. **97**, 59 (1985).
[32] B. Sheikholeslami and R. Wohlert, Nucl. Phys. **B259**, 572 (1985).
[33] S. Meinel (private communication).
[34] S. Beane, E. Chang, S. Cohen, W. Detmold, H. Lin, T. Luu, K. Orginos, A. Parreño, M. Savage, and A. Walker-Loud, Phys. Rev. D **87**, 034506 (2013).
[35] S. Beane *et al.* (NPLQCD Collaboration), Phys. Rev. C **88**, 024003 (2013).
[36] C. W. Bernard, T. Draper, K. Olynyk, and M. Rushton, Phys. Rev. Lett. **49**, 1076 (1982).
[37] G. Martinelli, G. Parisi, R. Petronzio, and F. Rapuano, Phys. Lett. B **116B**, 434 (1982).
[38] F. Lee, R. Kelly, L. Zhou, and W. Wilcox, Phys. Lett. B **627**, 71 (2005).
[39] F. X. Lee, L. Zhou, W. Wilcox, and J. C. Christensen, Phys. Rev. D **73**, 034503 (2006).
[40] C. Aubin, K. Orginos, V. Pascalutsa, and M. Vanderhaeghen, Phys. Rev. D **79**, 051502 (2009).
[41] W. Detmold, B. C. Tiburzi, and A. Walker-Loud, Phys. Rev. D **79**, 094505 (2009).
[42] W. Detmold, B. Tiburzi, and A. Walker-Loud, Phys. Rev. D **81**, 054502 (2010).
[43] T. Primer, W. Kamleh, D. Leinweber, and M. Burkardt, Phys. Rev. D **89**, 034508 (2014).
[44] H. Fiebig, W. Wilcox, and R. Woloshyn, Nucl. Phys. **B324**, 47 (1989).
[45] J. C. Christensen, W. Wilcox, F. X. Lee, and L.-m. Zhou, Phys. Rev. D **72**, 034503 (2005).
[46] M. Lujan, A. Alexandru, W. Freeman, and F. Lee, Phys. Rev. D **89**, 074506 (2014).
[47] W. Freeman, A. Alexandru, M. Lujan, and F. X. Lee, Phys. Rev. D **90**, 054507 (2014).
[48] G. 't Hooft, Nucl. Phys. **B153**, 141 (1979).
[49] M. J. Savage, Nucl. Phys. **A700**, 359 (2002).
[50] J.-W. Chen and M. J. Savage, Phys. Rev. D **65**, 094001 (2002).
[51] S. R. Beane and M. J. Savage, Nucl. Phys. **A709**, 319 (2002).
[52] M. Deka *et al.*, Phys. Rev. D **91**, 014505 (2015).
[53] J. Green, S. Meinel, M. Engelhardt, J. Laeuchli, J. Negele, K. Orginos, A. Pochinsky, and S. Syritsyn, Phys. Rev. D **92**, 031501 (2015).
[54] M. Albanese *et al.* (APE Collaboration), Phys. Lett. B **192**, 163 (1987).
[55] W. Detmold and K. Orginos, Phys. Rev. D **87**, 114512 (2013).
[56] B. Tiburzi and S. Vayl, Phys. Rev. D **87**, 054507 (2013).
[57] M. C. Birse, X.-D. Ji, and J. A. McGovern, Phys. Rev. Lett. **86**, 3204 (2001).
[58] Z. Shi, Ph.D. thesis, College of William & Mary, 2013.
[59] Z. Shi and W. Detmold, *Proc. Sci.*, LATTICE2011 (2011) 328.
[60] S. Beane, W. Detmold, K. Orginos, and M. Savage, Prog. Part. Nucl. Phys. **66**, 1 (2011).

[61] R. A. Briceño, Z. Davoudi, T. Luu, and M. J. Savage, Phys. Rev. D **88**, 114507 (2013).
[62] D. B. Kaplan, M. J. Savage, and M. B. Wise, Phys. Rev. C **59**, 617 (1999).
[63] J.-W. Chen, G. Rupak, and M. J. Savage, Nucl. Phys. **A653**, 386 (1999).
[64] S. R. Beane and M. J. Savage, Nucl. Phys. **A694**, 511 (2001).
[65] W. Detmold and M. J. Savage, Nucl. Phys. **A743**, 170 (2004).
[66] H. B. Meyer, arXiv:1202.6675.
[67] M. Lüscher, Commun. Math. Phys. **105**, 153 (1986).
[68] M. Lüscher, Nucl. Phys. **B354**, 531 (1991).
[69] S. Beane, P. Bedaque, A. Parreño, and M. Savage, Phys. Lett. B **585**, 106 (2004).
[70] M. Lüscher and U. Wolff, Nucl. Phys. **B339**, 222 (1990).
[71] D. Allor, P. Bedaque, T. D. Cohen, and C. T. Sebens, Phys. Rev. C **75**, 034001 (2007).
[72] T. Yamazaki, Y. Kuramashi, and A. Ukawa (PACS-CS Collaboration), Phys. Rev. D **81**, 111504 (2010).
[73] T. Yamazaki, K.-i. Ishikawa, Y. Kuramashi, and A. Ukawa, Phys. Rev. D **86**, 074514 (2012).
[74] T. Yamazaki, K.-I. Ishikawa, Y. Kuramashi, and A. Ukawa, *Proc. Sci.*, LATTICE2013 (2014) 230.
[75] J.-W. Chen and M. J. Savage, Phys. Rev. C **60**, 065205 (1999).
[76] G. Rupak, Nucl. Phys. **A678**, 405 (2000).
[77] A. Cox, S. Wynchank, and C. Collie, Nucl. Phys. **74**, 497 (1965).
[78] S. Reddy (private communication).
[79] R. G. Edwards and B. Joo (SciDAC Collaboration, LHPC Collaboration, UKQCD Collaboration), Nucl. Phys. B, Proc. Suppl. **140**, 832 (2005).
[80] M. Al-Hashimi and U.-J. Wiese, Ann. Phys. (N.Y.) **324**, 343 (2009).
[81] R. A. Briceño, Z. Davoudi, T. C. Luu, and M. J. Savage, Phys. Rev. D **89**, 074509 (2014).
[82] C. Lehner and T. Izubuchi, *Proc. Sci.*, LATTICE2014 (2015) 164.
[83] M. Engelhardt (LHPC Collaboration), Phys. Rev. D **76**, 114502 (2007).
[84] B. C. Tiburzi, Phys. Rev. D **89**, 074019 (2014).
[85] J. S. Schwinger, Phys. Rev. **82**, 664 (1951).